6

Physical Metallurgy and Material Systems of Laser Cladding

This chapter will describe the basic physical metallurgy applied to laser cladding and review the material systems that are being investigated for suitability in laser cladding processes. In the first section, the general cladability of substrate/clad materials will be described including both processing and metallurgical considerations. In the next section, a basic description of the relevant solidification conditions encountered during laser cladding will be completed. This will include the microstructural features that develop in the clad as a result of the solidification conditions. In the final section of the chapter, the material combinations that are most widely being investigated will be reviewed.

6.1 Cladability

There are many possible definitions of cladability. In this text, we consider cladability to include primarily the formation of a continuous, high density clad deposit with a uniform or homogeneous microstructure, possessing a strong metallurgical bond to the substrate but with low dilution. However, in particular cases, cladability could also include the requirement of a certain level of dilution by the substrate, a certain clad height or deposition efficiency or even specific materials properties that are required from the clad.

Using the above definition, cladability is primarily determined by the processing parameters used during the cladding operation as well as the metallurgical interactions or compatibility of the clad and substrate materials. Both these topics will be considered in detail in the following sections. The discussion in this section will limit itself to the powder injection method of laser cladding. However, the principles discussed can be equally applied to other laser cladding methods.

6.1.1 Processing Parameter Considerations

In order to achieve a dense clad that is metallurgically bonded to the substrate, enough energy must be delivered by the laser beam to the process volume such that the powder stream and a small volume of substrate surface melts. Because high temperature gradients are present in the melt pool, strong convection forces develop due to the Marangoni effect [35]. As a consequence, the liquid phases rapidly mix and become homogeneous. Upon cooling, this well-mixed liquid phase solidifies and forms the basis of the dense well-bonded clad layer.

The energy delivered to the process volume is not only determined by the laser beam energy but also by its spot size, the velocity of the substrate, and in the case of a pulsed laser, the frequency F and duration of the pulse W. The volume of material that this delivered energy must melt is determined by the powder feed rate and substrate velocity. As described in Section 2.6.2.2 of Chapter 2, these various process parameters can be combined into two effective parameters defined as the effective energy density E_{eff} [J/mm^2] and the effective powder deposition density ψ_{eff} [g/mm^2]. The role of these parameters in producing a dense clad with good bonding to the substrate can be demonstrated by an experimental case study as described below.

6.1.1.1 Case Study: FeAl Cladding on Mild Steel

In this case study, the cladding of FeAl on mild steel is investigated. The aim of this study was to obtain a correlation between combined process parameters with the clad bead quality (or cladability). However, it also demonstrates the potential of laser cladding a FeAl coating on mild steel.

Literature shows that iron-aluminide alloys for high temperature applications have been used for several years primarily due to their superior high temperature oxidation and sulfidation resistance [229, 230, 231, 232]. These alloys have improved electrical resistance, cyclic fatigue resistance, high temperature oxidation resistance, and both low and high temperature strength [233]. Its application in fuel cell technology has shown that it is extremely resistant to corrosion and metal loss when exposed to oxidizing atmospheres at high temperatures [234]. Furthermore, these alloys are lower in cost and have better corrosion resistance compared to conventional Ni-based and stainless steel type alloys [235].

In spite of the mentioned properties of the iron-aluminides, production of this alloy in bulk form is limited due to hydrogen-induced embrittlement. The possibility of producing the iron-aluminide coating on less corrosion-resistant materials, such as low carbon and stainless steels, has recently been investigated [230, 232]. These coatings were produced by weld overlay cladding processes using gas tungsten arc (GTA) and gas metal arc (GMA) welding techniques. The results indicate that at welding contents above 10 wt% Al, cold cracking in the iron-aluminide cladding occurs in a similar manner to that observed in bulk samples.

The advantages of laser cladding, including chemical cleanliness, localized heating, low dilution of the cladding material by the substrate and rapid cooling rates [101, 49], may provide the capability of production of iron-aluminide on mild steel to overcome some of the problems encountered in arc-welding based iron-aluminide coatings.

In the following sections, the results of experiments for production of iron-aluminide coating on mild steel will be addressed.

6.1.1.1.1 Experimental Setup and Procedure The powders used in this study were commercially pure Fe and Al powders (i.e., 98% pure) both with a mesh size of 45 μm (-325). The powders were mixed to a bulk composition of Fe - 20wt% Al by a dry milling procedure for one hour. Sandblasted mild steel plates (0.25 to 0.28 C; 0.6 to 1.2 Mn) with $200 \times 20 \times 5$ mm dimensions were used as the substrate. The laser was turned on 10 mm away from the edge of the plate.

The experiments were performed with a LASAG FLS 1042N Nd: YAG laser with a maximum power of 1000-W, 9MP-CL Sulzer Metco powder feeder, and a 4-axis CNC table. The laser beam and powder feed nozzle were stationary while the CNC table moved the substrate at a controlled velocity. An argon shield gas was fed along the powder stream. It was also used to protect the optical lenses. During the various laser-cladding experiments, clad height was measured in real-time using the CCD-based detector as explained in Chapter 5.

Initial experiments were performed to investigate the influence of laser processing characteristics on the cladding process. The conditions studied are given in Table 6.1, where F is the laser pulse frequency [Hz], W the laser pulse width (duration) [ms], E the pulse laser energy [J] and U is the process speed [mm/s]. The other process parameters were constant for all experiments as listed in Table 6.2.

Each condition was performed along a track. For Conditions 1 to 14, E was changed incrementally as shown in Figure 6.1, while F, W, and U were constant. For Conditions 15 to 19, F was changed as shown in Figure 6.2, while E, U, and W were fixed.

As indicated in Table 6.1, Conditions 1 to 6 were used to determine the influence of laser pulse energy and process speed on the Fe-Al cladding process. Also, Conditions 7 to 11 and Conditions 12 to 14 were performed to investigate the same effects with different laser pulse widths and laser pulse frequencies. Experiments 15 to 19 were used specifically to explore the influence of the laser pulse frequency.

Representative samples from experiments with a given set of process parameters were sectioned, mounted and polished, and metallurgical analysis of these samples were performed using optical microscopy to determine the clad bead quality as a function of the processing parameters.

TABLE 6.1
Laser processing parameters.

Cond.	Pulse Frequency [Hz]	Pulse Width [ms]	Pulse Energy [J]	Process Speed [mm/s]
1	100	3.0	2 to 4	0.75
2	100	3.0	2 to 4	1.00
3	100	3.0	2 to 4	1.25
4	100	3.0	2 to 4	1.50
5	100	3.0	2 to 4	1.75
6	100	3.0	2 to 4	2.00
7	80	4.1	2 to 4	0.75
8	80	4.1	2 to 4	1.00
9	80	4.1	2 to 4	1.25
10	80	4.1	2 to 4	1.50
11	80	4.1	2 to 4	1.75
12	50	6.4	2 to 4	1.00
13	50	6.4	2 to 4	1.25
14	50	6.4	2 to 4	1.50
15	40 to 100	3.0	4	1.00
16	40 to 100	3.0	4	1.50
17	35 to 95	3.0	5	1.25
18	35 to 95	3.0	5	1.5
19	35 to 95	3.0	5	1.75

TABLE 6.2
Additional process parameters, which were fixed for all conditions.

Laser shield gas (m^3/s)	2.34e-5
Laser spot radius on workpiece(mm)	0.7
Powder feed rate (g/min)	1
Powder feeder shield gas(m^3/s)	2.34e-5
Powder stream diameter on the workpiece (mm)	1.6
Nozzle angle (deg)	55

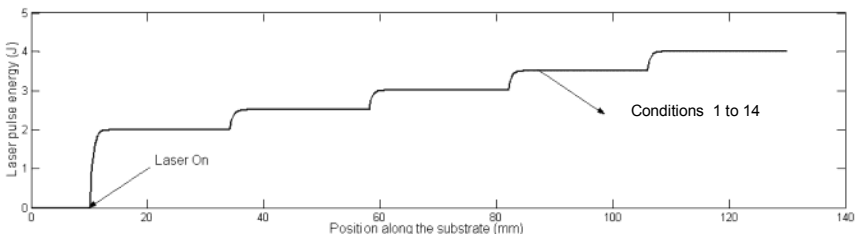

FIGURE 6.1
Multistep laser pulse energies for Conditions 1 to 14.

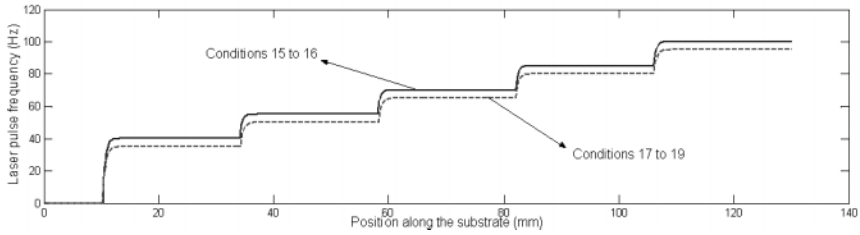

FIGURE 6.2
Multistep laser pulse frequencies for Conditions 15 to 19.

6.1.1.1.2 Results The optical CCD-based detector provides continuous height measurements of the clad along the substrate as described in Chapter 3. The continuous measurement of the clad height offers valuable information about the surface roughness of the clad deposit, which can be used in evaluation of the clad bead quality. Figure 6.3 shows the continuous clad height measurements for two typical results associated with Conditions 1 and 4.

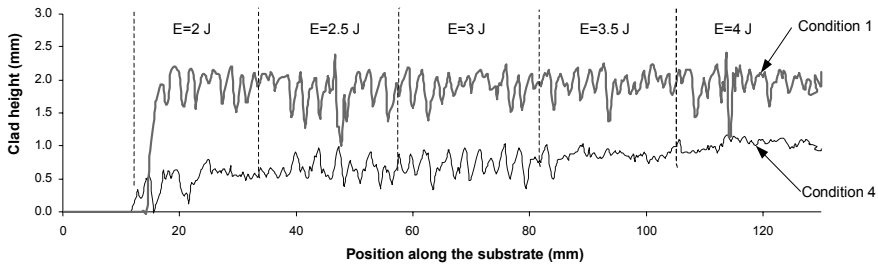

FIGURE 6.3
Clad heights along the substrate for Conditions 1 and 4.

The roughness of both samples can also be determined by analyzing the measured clad height. Figure 6.3 indicates that the roughness of the clad was high for Condition 1 along the entire track with an average deviation of 0.43 mm. For Condition 4, the clad roughness was fairly good with deviation of 0.1 mm for the last two steps, when $E = 3.5$ J and $E = 4.0$ J. The corresponding macrostructure of the track region for Condition 4 at $E = 4.0$ J is shown in Figure 6.4. Also, Figure 6.5 shows the corresponding track macrostructure for Condition 1 at $E = 3.5$ J.

For Conditions 1 and 4 at $E = 2.0$ J and $E = 2.5$ J, the quality of clad product was poor in terms of strength of bonding between the clad and substrate.

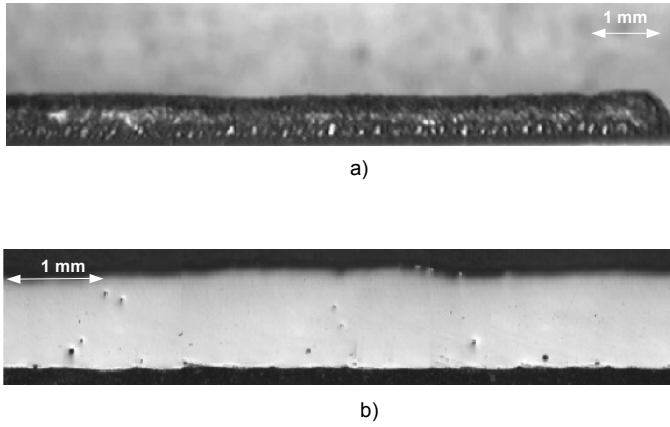

FIGURE 6.4

a) Longitudinal view of the macro-quality of a clad with good surface condition before polishing, b) longitudinal section of the macro-quality of the clad indicating good qualities (Condition 4 at $E = 4.0$ J).

For these cases, the clads were easily removed from the substrate following the process.

The bond strength of the other part of a track at $E = 3.0$ through 4 J was tested by a simple bending experiment [236]. During the bending test, no separation was observed. However, some cracks were created after the clad and substrate were bent about 40° relative to the substrate as seen in Figure 6.6. As the figure shows, the cracks continue through the clad and end in the substrate with no cracks running along the substrate interface providing further evidence of a strong bond between the clad and substrate. The bending test for other parts of a track with lower energy ($E = 2.0$ and $E = 2.5$ J) showed a weak bond between the clad and substrate such that the clad was separated from the substrate.

Clearly the clad height measurements made in real-time with the optical CCD-based detector relate directly to the clad quality produced. A smooth clad deposit with little porosity and a good bond with the substrate corresponds with the detector readings, which indicate little height variations. Conversely, the detector readings, which indicate large height deviations correspond to rough clad deposits with a significant level of porosity.

The above-mentioned procedure was carried out for other samples. The obtained information will be then used in the development of a strategy for evaluation of the clad bead quality later.

In the following subsections, we use the average of the measured clad height

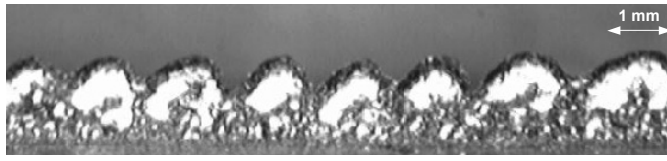

a)

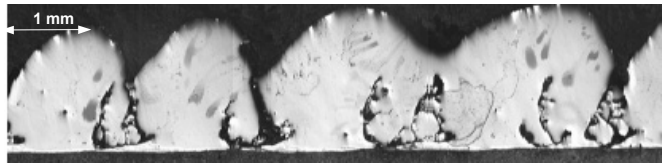

b)

FIGURE 6.5
a) Longitudinal view of a clad with high roughness, b) longitudinal section of a clad with high roughness (Condition 1 at $E = 3.5$ J).

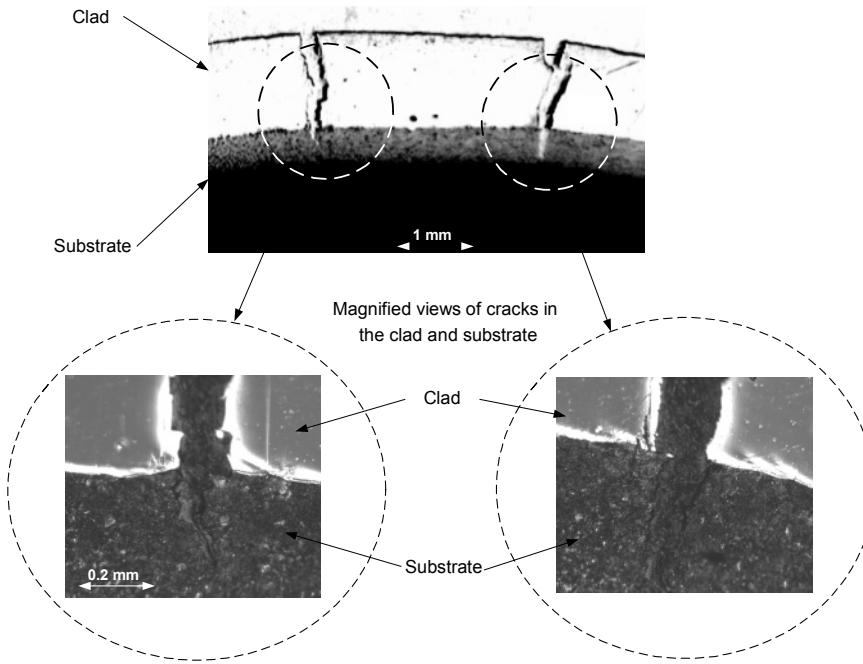

FIGURE 6.6
Bending section of a track at $E = 3.0$ through 4.0 J.

at any portion of the track with constant laser pulse energy or frequency to investigate the influence of process parameters, including process speed, laser pulse shaping, average power and duty cycle on the clad height.

6.1.1.1.3 Influence of Laser Pulse Shaping and Process Speed on Average Clad Height Due to the repetitive nature of the laser beam generated by the Nd:YAG pulsed laser, two parameters were defined as duty cycle and average laser power, which are expressed by Equations (2.4) and (2.5), respectively. These two parameters are usually used to study Nd:YAG pulse laser-based experiments. In this section, we use these two parameters to study their effects on the average clad height.

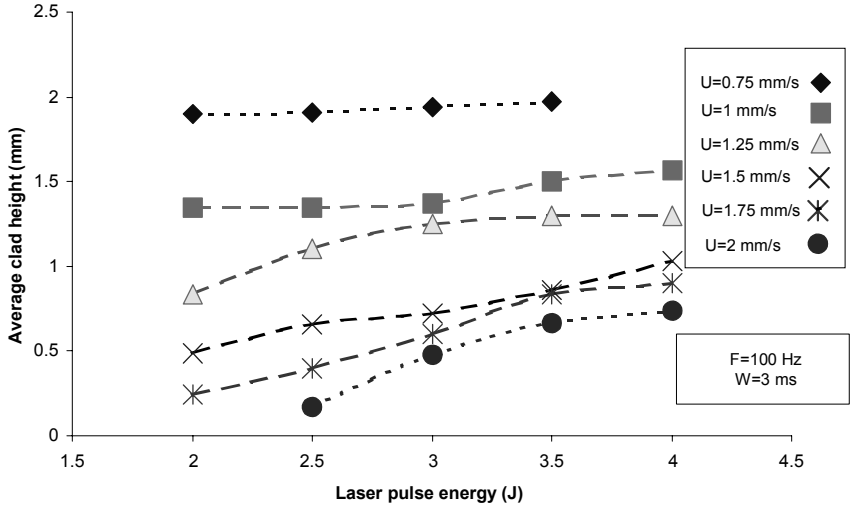

FIGURE 6.7
Fe-Al average clad height as a function of laser pulse energy and process velocity (C is fixed, P_l is variable).

Figure 6.7 illustrates the effect of laser pulse energy and process velocity on the average clad height while the laser pulse frequency and width are both constant, and, as a result, duty cycle is also fixed. The results confirm that as U decreases or E increases the clad height increases. The figure confirms the consistency in the process when the laser pulse energy or process speed are changed.

The other issue of interest is the influence of the laser pulse frequency on the

average clad height. Figure 6.8 shows the influence of laser pulse frequency and process speed on the average clad height while the laser pulse energy and width are set to 5 J and 3.00 ms, respectively. The figure confirms a consistent nature for the process for the experiments explored. As U increases the clad height decreases, whereas if F increases the clad height increases.

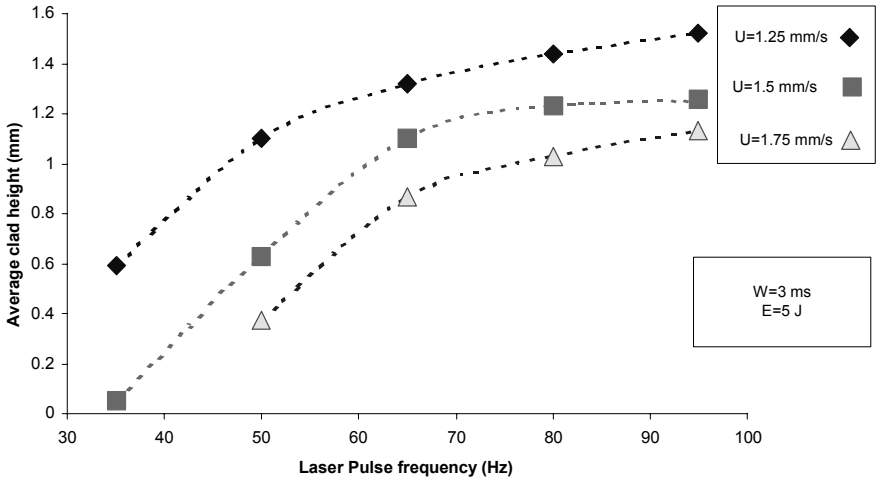

FIGURE 6.8

Fe-Al average clad height as a function of laser pulse frequency and process speed (C and P_l are both variable).

Figure 6.9 shows the influence of laser pulse energy and frequency on the average clad height while the process speed and laser pulse width are both constant. As seen for the conditions explored, an increase in both E and F causes the average clad height to increase as well.

From Figures 6.8 to 6.9, it can be concluded that the clad height increases with either an increase in duty cycle or average power as determined by a variation in E and F or both.

Figure 6.10 reports average clad height data for the case in which C and U are both fixed, but W and F are both varied. The figure indicates that the nature of the process is not consistent. Despite a fixed duty cycle, different combinations of the laser pulse frequency and width do not result in the identical clad heights. However, as E decreases, the clad height also decreases. The same behavior occurs with respect to F except for the condition with $F = 50$ Hz and $W = 6.4$ ms. Although the clad height for this condition is relatively close to the condition with $F = 100$ Hz and $W = 3.0$ ms, the clad quality is poor for the entire track in terms of bonding between the clad and

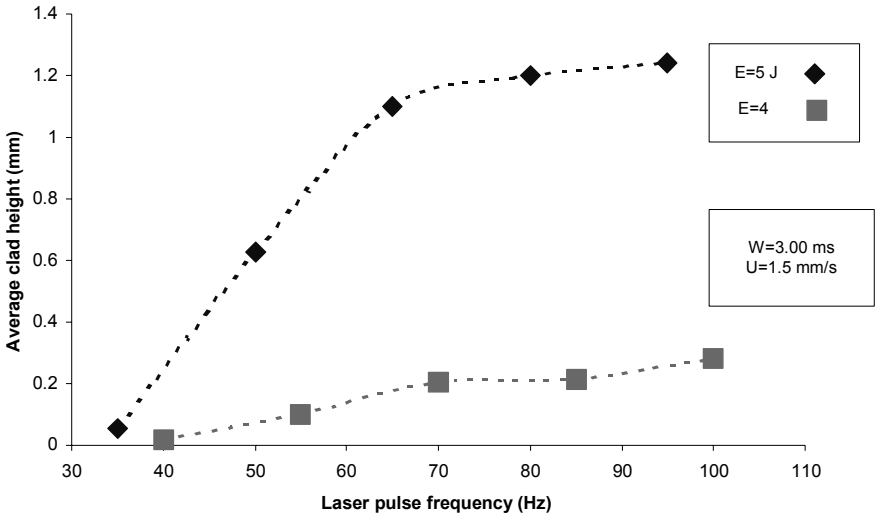

FIGURE 6.9
Fe-Al average clad height as a function of laser pulse frequency and energy (P_l and C are variable).

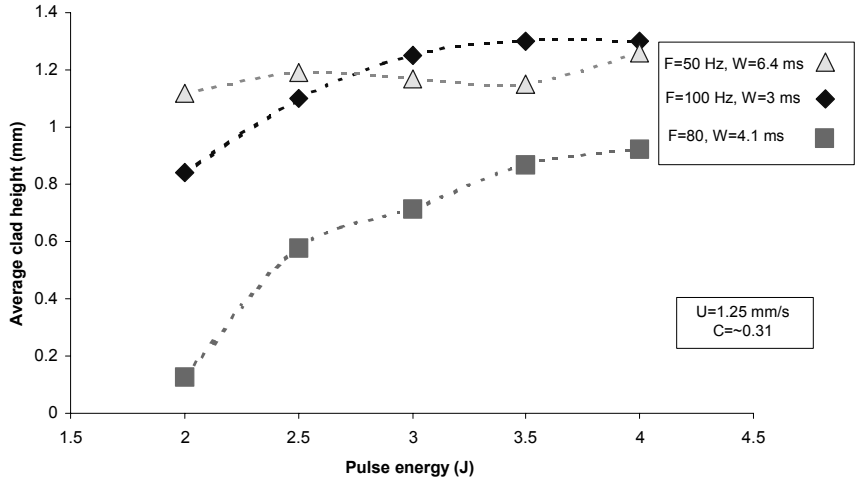

FIGURE 6.10
Fe-Al average clad height as a function of laser pulse energy, frequency and width while the duty cycle is constant (C is fixed, P_l is variable).

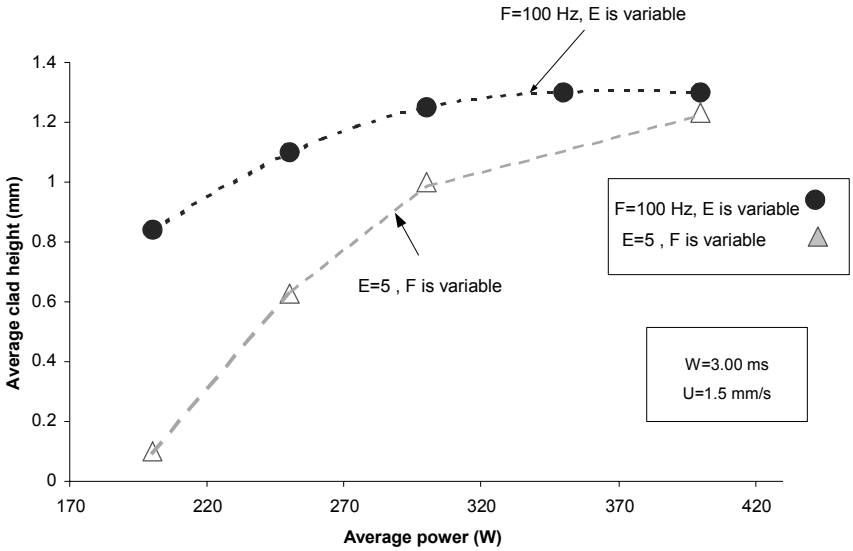

FIGURE 6.11

Dependency of the Fe-Al average clad height on the average power at different laser pulse energies and frequencies.

substrate.

Figure 6.11 shows the influence of the average power on clad height when using different process parameters. The results show an inconsistency in the process as the average power is selected for the clad height evaluation. For instance, at condition $E = 5.0$ J and $F = 40$ Hz the average power is 200 W which is identical to the situation where $E = 2.0$ J and $F = 100$ Hz; however, the generated heights are significantly different. The main reason of this behavior is the interaction of powder stream and the laser pulses and its contribution to the clad generation. Of interest is the fact that at the lower frequencies (lower duty cycle), the interaction time between the laser beam and powder particles decreases. Consequently, the rate of effective powder deposition decreases. As is evident in the figure, the influence of this reduces significantly at higher frequencies and energies.

All the previous figures indicate the dependencies of the process on the various parameters. Although the figures provide valuable insight into the process, the evaluation of the clad quality may be difficult to be described using them due to the variety of parameters involved. As a result, we develop a strategy by introducing combined parameters and their influence on the bead quality of clad, which will be addressed in the last section of this chapter.

6.1.1.1.4 Clad Substrate Macro/Microstructure and Hardness In the previous section, two different qualities of clads were addressed: clads with good surface roughness and strong clad/substrate bonds, and clads with poor surface roughness and weak clad/substrate bonds. To further investigate the clad/substrate macrostructures for these two possible types of cladding, sections through the clad/substrate couples in transverse and longitudinal directions were made.

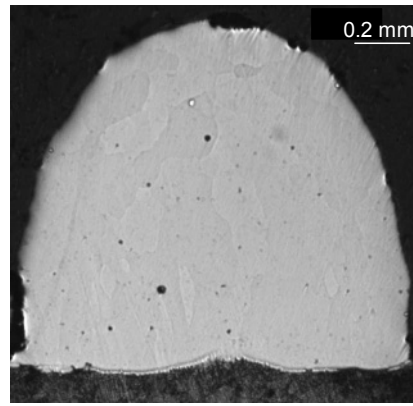

FIGURE 6.12
Macrostructure of transverse section of clad made using $E = 4.0$ J, $W = 3.0$ ms, $F = 100$ Hz and $U = 1.5$ mm/s.

Figures 6.12 and 6.13 show the clad/substrate macrostructure for a sample with $E = 4.0$ J, $W = 3.0$ ms, $F = 100$ Hz, and $U = 1.5$ mm/s in transverse and longitudinal sections. The clad deposit and grain boundaries are clearly visible. The clad has a good profile. The figures indicate that this condition produces a very dense clad with homogeneous structure and negligible porosity. In addition, no cracks were observed in the clads or at the clad/substrate interface. Furthermore, the microstructure of the clad in longitudinal section can be explored through Figure 6.13. It is evident from the figure that two structures exist in the clad microstructure. The first structure is the lines of banding which are parallel to the solid/liquid interface. The banding structure is generated due to the repetitive pulsing nature of the heat source used in the process. In the rapid solidification, the absence and presence of the heat source in a short period of time cause an oscillatory growth of the solid area. This oscillatory growth results in the composition deviation [237]. The second structure is the grain boundaries in the clad region. As seen, nucleation starts from the substrate/clad interface, and the grains grow normal to the

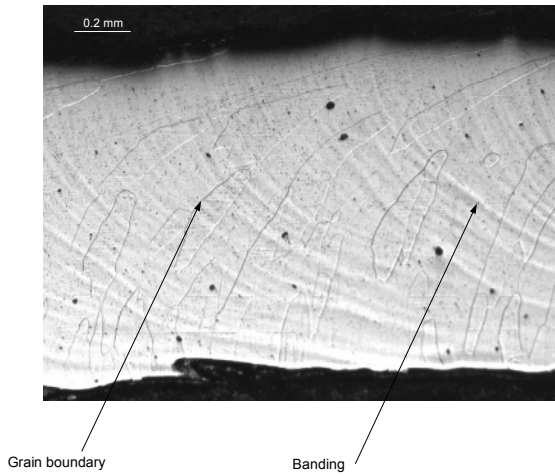

FIGURE 6.13
Macro/microstructure of longitudinal section of clad made using $E = 4.0$ J, $W = 3.0$ ms, $F = 100$ Hz and $U = 1.5$ mm/s.

solid/liquid interface (the lines that are indicated by the banding structure).

Figures 6.14 and 6.15 show the clad/substrate macrostructure for a sample with $E = 2.0$ J, $W = 3.0$ ms, $F = 100$ Hz, and $U = 1.5$ mm/s in transverse and longitudinal sections, respectively. Conversely, this sample exhibits a very porous deposit which is poorly bonded to the substrate.

The hardness of the clad shown in Figure 6.12 was measured across the bond area using a Vickers microhardness instrument. The results are shown in Figure 6.16. Clearly, the hardness on the clad deposit is much higher than that of the mild steel substrate. The hardness steadily rises within the heat-affected zone (HAZ) of the substrate until it reaches a value two times higher than the substrate, in the clad deposit. The clad hardness is significantly higher than the hardness that is reported for the arc weld overlay techniques [230, 231].

6.1.1.1.5 Combined Parameters Calculated values for E_{eff} and ψ_{eff} using Equations (2.8) and (2.9), respectively, for the processing Conditions 1 to 14 are plotted in Figure 6.17, and for Conditions 15 to 19 are plotted in Figure 6.18.

Based on continuous clad height measurement, optical microscopy of selected sectioned clads, bending test, observations, and the evidence represented earlier, four regions are distinguishable. These regions are labeled as follows:

1. **Good quality clad:** The selected E_{eff} and ψ_{eff} in this region pro-

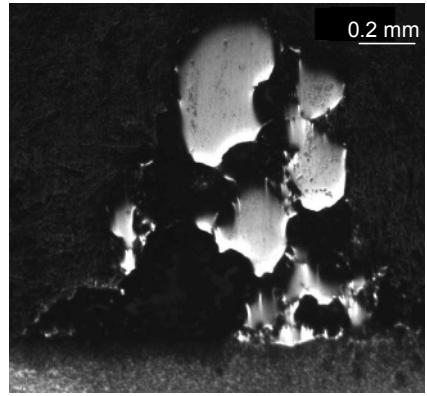

FIGURE 6.14
Macrostructure of transverse section of clad at $E = 2.0$ J, $W = 3.0$ ms, $F = 100$ Hz, and $U = 1.5$ mm/s.

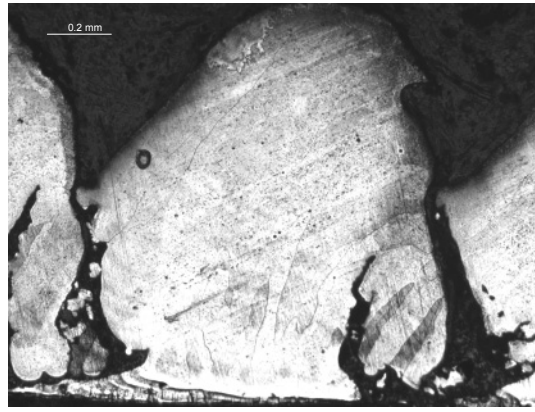

FIGURE 6.15
Macro/microstructure of longitudinal section of clad at $E = 2.0$ J, $W = 3.0$ ms, $F = 100$ Hz, and $U = 1.5$ mm/s.

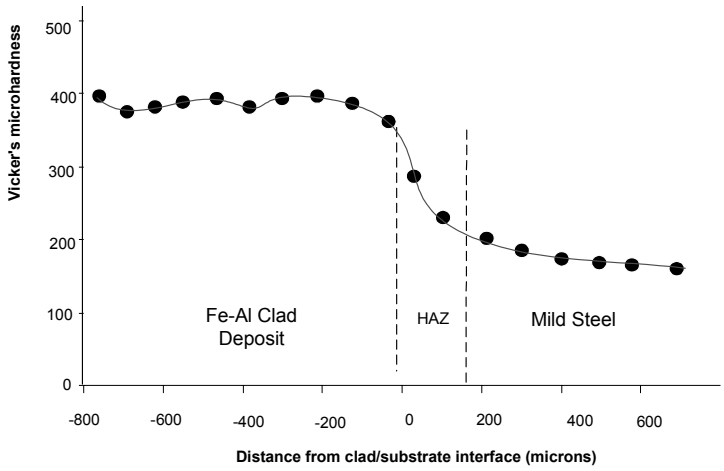

FIGURE 6.16
Microhardness of clad specimen made using $E = 4.0$ J, $W = 3.0$ ms, $F = 100$ Hz, and $U = 1.5$ mm/s.

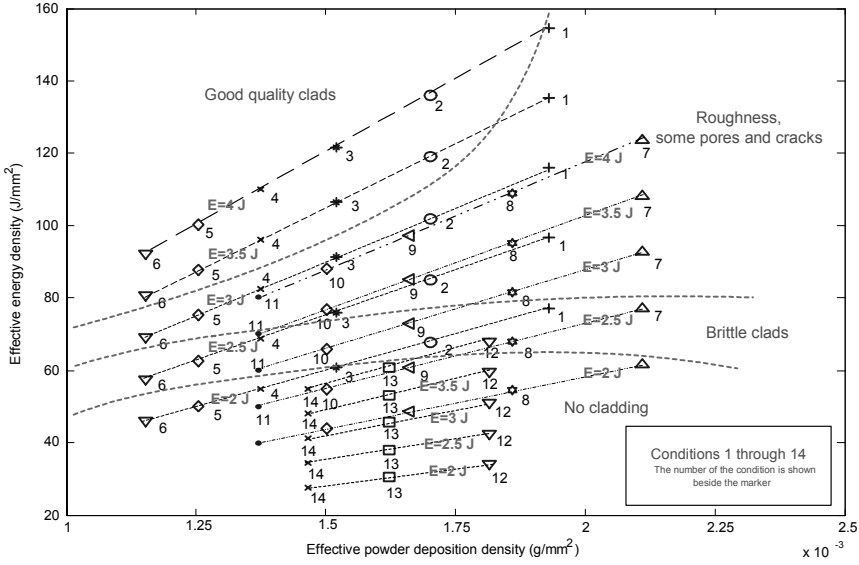

FIGURE 6.17
Effective energy density versus effective powder deposition density for Conditions 1 to 14.

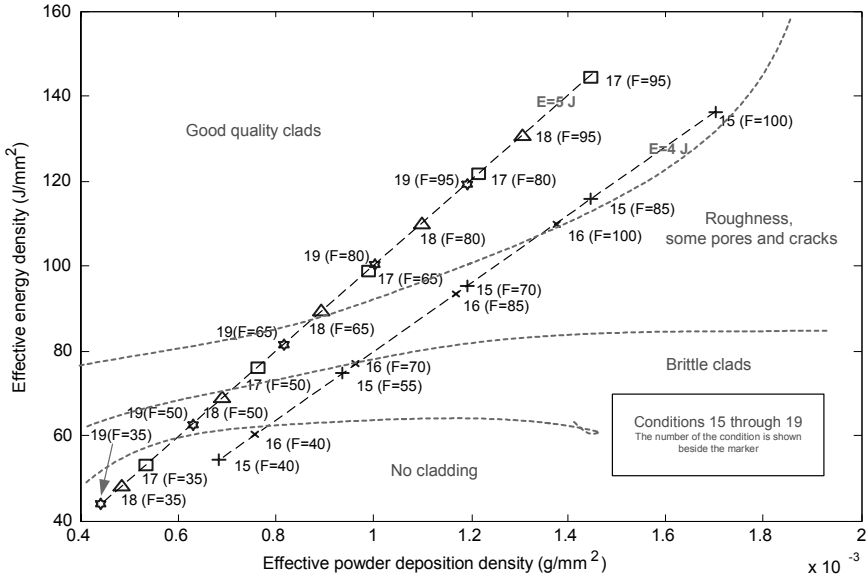

FIGURE 6.18
Effective energy density versus effective powder deposition density for Conditions 15 to 19.

vide clads with a good bond between the substrate and clad where the clads have a smooth surface and good profile without cracks and pores. Figures 6.4, 6.12, and 6.13 show an example of this type of clad. The figures indicate that the parameters in this region produce a very dense clad with homogeneous structure, no cracks, and negligible porosity.

2. **Roughness, some pores and cracks**: In this region, the clad has a good bond with the substrate; however, its surface is not smooth and many bumps are observed along the track. Figures 6.5, 6.14, and 6.15 show an example of this type of clad. The figures indicate that the parameters selected in this region produce a clad with high roughness, as well as porosity and cracks.

3. **Brittle clads**: In this region, a clad exists; however, there is not a good bond between the clad and substrate. The clad in this region is easily removed by hand after the process.

4. **No cladding**: In this region, no clad can be created due to the significant lack of energy.

Generally, Figures 6.17 and 6.18 can be used for clad bead quality evaluation. However, the range of validity of Figures 6.17 and 6.18 is $0.4 \leq U \leq 3.0$

[mm/s], $35 \leq F \leq 100$ [Hz], $2.0 \leq E \leq 5.0$ [J], $3.0 \leq W \leq 5.0$ [ms], $\dot{m} = 1$ g/min, and $D = 1.4$ mm.

As seen in Figures 6.17 and 6.18, a critical state exists in the iron-aluminide laser cladding process which should be met during the real-time control of laser cladding to produce a good quality clad and high cladability.

6.1.2 Metallurgical Considerations

The formation of a strong bond between the clad and substrate material also depends critically on the metallurgical interactions that take place between the two materials during the cladding process. There will be certain cases where incompatibility between the substrate and clad materials will make it virtually impossible for a strong bond to be formed, in which case cladability will be nonexistent. Even in cases where strong bonding can be achieved, the metallurgical reactions between the clad and substrate materials will have an important contribution to the actual values of E_{eff} and ψ_{eff} that are required to achieve an optimum clad. Therefore, it is important to understand the details of these metallurgical interactions so that intelligent material selections can be made when choosing a clad and a substrate couple, and in predicting and interpreting the resulting clad microstructure.

Laser cladding is essentially an extremely rapid and localized alloying process, which takes place between the clad material and substrate. Normally the objective in laser cladding is to minimize alloying or dilution of the clad by the substrate. However, the requirement of a strong metallurgical bond means that alloying or dilution cannot be avoided entirely and must be carefully controlled.

Before discussing metallurgical interactions, it is first necessary to understand the physical circumstances under which alloying takes place during laser cladding. Figure 6.19 illustrates a schematic of the melt pool created during laser cladding of pure B powder onto a pure A substrate. In this figure, it is assumed that the cladding process has reached a steady-state; the laser beam and powder stream simultaneously come into contact with the melt pool, which has been created by the molten clad/substrate couple. A portion of the energy from the laser beam melts a small volume of the substrate at the leading edge of the clad/substrate couple region X. A portion of the laser beam energy is also used to heat up the powder entering the process volume. Depending on the melting point of the powder, when it comes into contact with the melt pool it may be in the form of molten droplets or solid particles. In many circumstances, there are likely both liquid and solid powder particles that come into contact with the melt pool surface. Therefore alloying (or mixing) will be between liquid A and liquid and/or solid B.

It is fairly well accepted that the high temperature gradients present in the melt pool during laser cladding set up intense convection due to the Marangoni effect [35, 238]. This leads to rapid homogenization or alloying within the melt pool. Convection in the liquid pool can be characterized by the surface tension

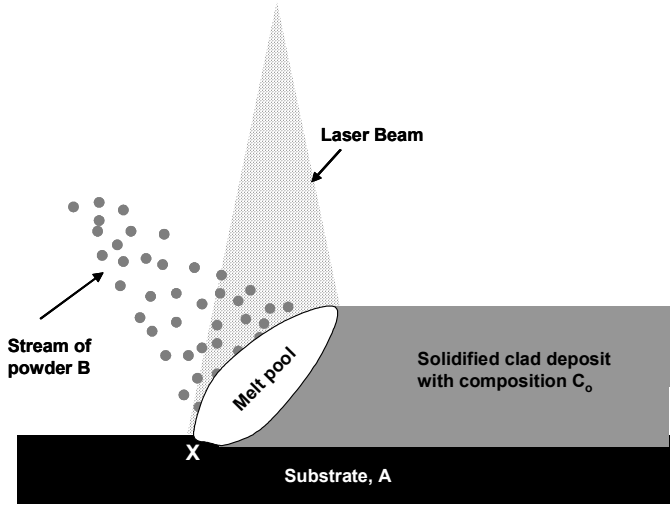

FIGURE 6.19
Schematic of the melt pool in laser cladding where alloying of the constituents occurs.

number S, which is equal to [35, 239]

$$S = \frac{(d\gamma/dT)qd}{\mu UK} \tag{6.1}$$

where $d\gamma/dT$ is the derivative of surface tension with respect to temperature [N/m·K], q is the total absorbed power per area of the substrate irradiated by the laser [W/m^2], d is the diameter of the laser beam on the substrate [m], μ is the viscosity of the melt pool [kg/s·m], U is the scanning speed of the laser beam (or substrate speed) [m/s], and K is thermal conductivity [W/m·K].

When $S \leq 45,000$ [158], convection is negligible; otherwise, convection is important. Clearly, the importance of convection is determined in large part by the physical properties of the materials making up the clad melt pool. Therefore, its contribution to mixing and alloying should be assessed for every material system in use. For example, while convection is generally accepted to be important, at least one detailed calculation by Almeida et al. [239] indicates that for a Nb-Al cladding couple, S was less than $45,000$ indicating that convection did not play a major role in the mixing process in this situation.

Regardless of the mechanisms of mixing or alloying, the results of the process can be initially understood by referring to a few simple metallurgical cases as depicted in Figure 6.20. In these cases, the substrate and/or powder stream could be considered to be pure A and B or pure B and A, respectively or pure C and D or pure D and C, respectively. The figure considers two cases:

1. Simple eutectic binary alloy system formed between A and B,

2. Simple isomorphous binary alloy system formed between C and D.

In most laser cladding situations, the melting point (T_m) of the clad and substrate materials will be different, and this is reflected in the hypothetical phase diagrams where the T_m of $A < B$ and T_m of $C < D$. In the following, these cases are explained.

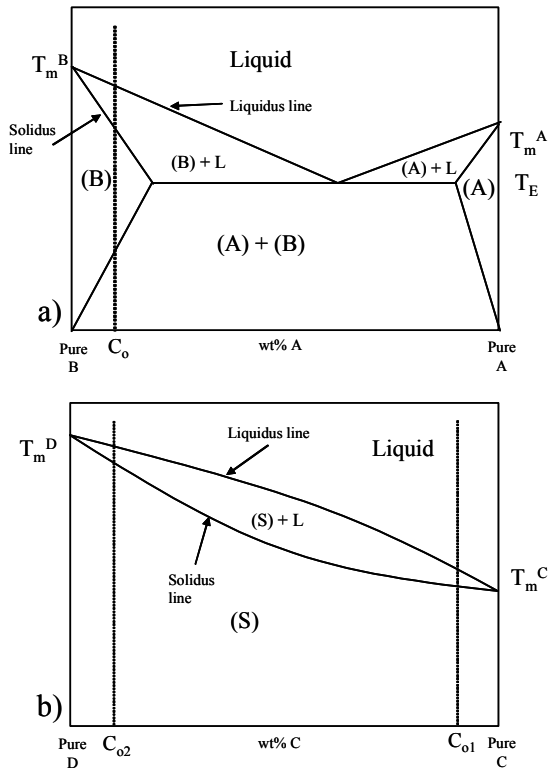

FIGURE 6.20
Hypothetical phase diagrams for a) simple eutectic, b) simple isomorphous binary alloy mixture.

6.1.2.1 A Simple Binary Eutectic Cladding Process

First, a cladding process where the clad powder is made of pure B and the substrate of pure A is considered. By design, dilution by the substrate will

be low, and therefore the bulk composition of the melt pool C_o would be on the B rich side of the phase diagram. As will be discussed in Section 6.2, it is well recognized that the melt pool in laser cladding is not at equilibrium, and therefore cannot be quantitatively characterized by an equilibrium phase diagram [204]. More specifically under non-equilibrium conditions, the liquidus and solidus lines usually shift toward each other with a subsequent reduction in the partition coefficient. However, the equilibrium phase diagram is still a useful tool in interpreting the general metallurgical interactions qualitatively that will take place during alloying in the melt pool of a laser cladding process.

Consider the solid/liquid interfacial region X, where the solid A substrate is in contact with the melt pool. Because solid-state diffusion is very slow compared to the process time in laser cladding, diffusion of solute B from the melt pool into the solid substrate is negligible. However, there will be a non-equilibrium partition coefficient k_v established between the solid and liquid phases. In a eutectic system, alloying reduces the melting point compared to the pure constituents. Therefore, melting of the substrate ahead of the melt pool will be assisted by compositional dissolution into the molten pool. This should have the effect of reducing the laser beam energy required to reach a condition of cladability as described in Section 6.1.1.

A similar conclusion can be made when examining the solid/liquid interfacial region between the melt pool and any unmelted pure B powders colliding with its surface. A non-equilibrium partition coefficient k_v will be established between the solid A particles and liquid phase. Again, in this eutectic system, melting of the solid B powder at the melt pool surface will be assisted by compositional dissolution into the molten pool, further reducing the laser beam energy required to reach a condition of cladability. This consequence of alloying, together with the fact that A and B exhibit good solubility in the liquid state, will create a situation of high cladability between either a pure A substrate and pure B powders or a pure B substrate and pure A powders.

6.1.2.2 A Simple Binary Isomorphous Cladding Process

Solubility between pure elements in an isomorphous system is also very good both in the liquid and solid states. Therefore, it may be expected that a system of this type would exhibit good cladability. However, the consequence of alloying on the melting point is very different than in a eutectic system and this could cause cladability problems depending on different selection of elements for the substrate and the powder.

The first case to consider is that where the substrate is made of the higher melting point pure D and the powder the lower melting point pure C. Again, with the assumption that low dilution of the clad by the substrate is desired, it is considered that the molten pool will have a C rich composition close to C_{o1}. Consider the solid/liquid interface at the leading edge of the clad track where the solid D substrate is in contact with the melt pool. In an isomorphous system, alloying of D with C reduces its melting point. Therefore, alloying

will assist the melting of the substrate layer by compositional dissolution into the molten pool and improved cladability.

An opposite conclusion can be made when examining the solid/liquid interfacial region, where solid C particles come into contact with the melt pool. In this case, alloying of C with the melt pool will raise its melting point. However, in order to have a sustainable molten zone with a composition of C_{o1} the melt pool temperature would have to be above the non-equilibrium liquidus temperature for that composition (and therefore above the melting point of the pure C powder). Therefore, the pure C particles will undergo dissolution into the pool provided the local composition remains above C_{o1}. Consequently this type of clad couple should exhibit good cladability, although the nature of the alloying will not reduce the process conditions necessary to produce a good clad to the extent of that expected in a eutectic system.

The second case to consider is that where the substrate is made of the lower melting point pure C and the powder, the higher melting point pure D. The requirement for low dilution is made such that the molten pool will have a D rich composition close to C_{o2}. Consider the solid/liquid interface region X of Figure 6.19, where the solid C substrate is in contact with the melt pool. Alloying with the melt pool will raise the melting point of the substrate, and therefore compositional dissolution will not assist in substrate melting.

Alloying of unmelted D particles with the melt pool of composition C_{o2} would lead to compositional dissolution of the powders and therefore assist in their melting. However, if the desired bulk composition of the clad is C_{o2}, then the temperature of the process volume must be relatively high and close to the melting point of the pure D powder. This requirement for a high melt pool temperature will tend to create excessive melting of the lower melting point C substrate and cause undesirable levels of dilution. Therefore, while a cladding couple of this type may exhibit good cladability from the point of view of a dense clad and good bond formation, it may not be cladable if a very low dilution is required, particularly if the melting points of C and D are very far apart.

6.1.2.3 Complex Multi-Component Alloy Systems

The above discussion points out that metallurgical interactions occurring between the substrate and powder stream can assist or hinder the cladding process through an alteration of the melting temperature of the melt pool. In addition, large differences between the melting point of the two starting constituents can lead to difficulties in controlling the degree of dilution and lead to high process temperatures and, therefore, high energies required to be delivered by the laser beam. However, in all of the above cases, a processing condition for good cladability, in terms of a continuous, dense clad and the establishment of a strong metallurgical bond between the clad and substrate, should be achievable. This will not always be the case for more complex alloy systems where intermediate phases can form as a result of alloying between

the substrate and powder. One of the major industrial applications of laser cladding is to create a hard, wear-resistant coating on a softer, more ductile substrate [35]. Unfortunately, this usually means that the melting point of the substrate and clad material are very different, and this tends to result in a complex phase diagram with several intermediate phases forming when the two elements are combined.

The hypothetical phase diagram of Figure 6.21 is an example of such a phase diagram where intermediate, intermetallic compounds α and β can form through alloying between pure E and F. In addition, elements with such large differences in melting point also exhibit low solubility with each other. Depicted in Figure 6.21 is a case where there is essentially no solubility of element F in E in the solid state as well as in the liquid state except at very high temperatures. Binary alloy systems with phase diagrams similar to this include Nb-Al, Ni-Al, Co-Al, Cr-Al and Fe-Al.

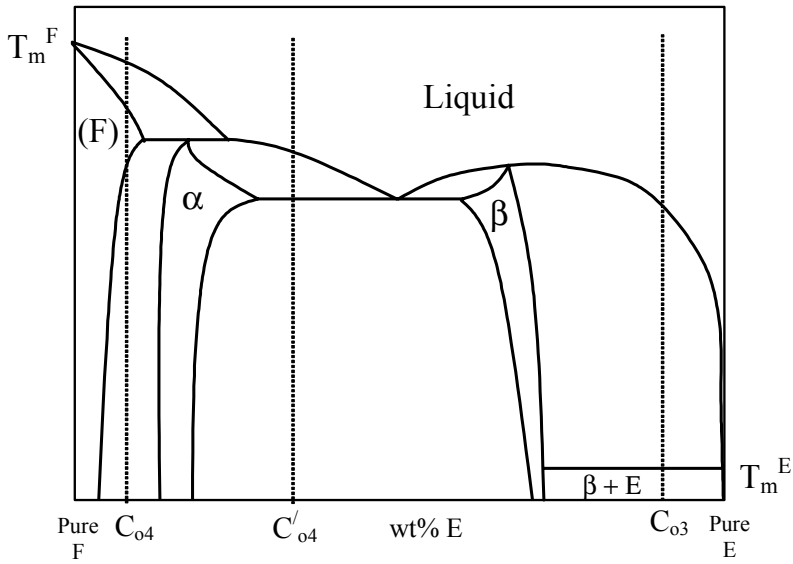

FIGURE 6.21
Hypothetical phase diagram of a binary system where alloying between the pure constituents (i.e., F and E) leads to the formation of intermediate (or intermetallic) phases.

As discussed in the previous section, the success of the process will depend on the objectives of the cladding operation including the composition of the substrate, powder, and the desired composition of the as deposited clad.

Therefore, several cases must be treated to fully explore cladability in alloy systems of this kind. The first case that will be considered is one where the substrate is made from the low melting point element E and the powder made from the high melting point element F. The requirement for low dilution is made such that the molten pool will have an F rich composition close to C_{o4}. If the melting points of the two elements are very far apart it will be very difficult to melt element F without causing excessive melting of the substrate material. Alloying of F particles, which come into contact with the melt pool, can result in compositional dissolution and this could help to melt the F particles. However, the melt pool temperature would have to be maintained at a very high level for a bulk composition of C_{o4} to be sustained. This would lead to excessive melting of the substrate and high dilution levels. The clad composition could shift toward C'_{o4} and, upon solidification, the clad would consist entirely of brittle α and β intermetallics. This would result in a poor bond with the substrate and poor cladability. The authors are aware of only one study that investigates the cladding situation described above. Li et al. [76] attempted to clad a Co-Cr rich alloy powder (i.e., Stellite 6) onto an Al-Si substrate. Over 90 wt% of the clad alloy is represented by Co and Cr while over 90 wt% of substrate is Al. Therefore, a qualitative understanding of the alloying expected between the substrate and powder can be interpreted by inspection of the Co-Al and/or Cr-Al binary phase diagrams (see Figures 6.22 and 6.23). Both binary alloys have a complex multi-component phase diagram similar in nature to the hypothetical phase diagram of Figure 6.21, including the formation of intermetallic compounds and very different melting points between Co (or Cr) and Al. The results of Li et al. [76] indicate that this system exhibits very poor cladability including difficulties in establishing process parameters, the formation of intermetallic compounds at the substrate/clad interface and excessive cracking in the bond region during cooling.

6.1.2.4 Case Study: Cladding of Nb on Al

Other conditions that have been reported with differing degrees of success are those where the composition of the clad deposited on the low melting point substrate has an E rich composition close to C_{o3} of Figure 6.21. Clad couples that have been investigated under these conditions include Nb-Al, Fe-Al, Ni-Al. The work on Nb-Al offers an excellent case study of what can occur under theses cladding conditions.

In practical circumstances, some of the above problems can be somewhat overcome and a cladding of practical use can be produced. An example of this is the case of cladding Nb on Al, which has been studied by several researchers [239, 77, 240, 241]. The Nb-Al phase diagram is depicted in Figure 6.24. As indicated, the melting point of Nb is 2469°C whereas that of Al is 661°C. Clearly the production of a Nb rich melt pool would be excessively difficult due to the high temperatures required. For example, even with alloying up to 10 wt% Al requires a melt pool temperature in excess of 2000°C. Some

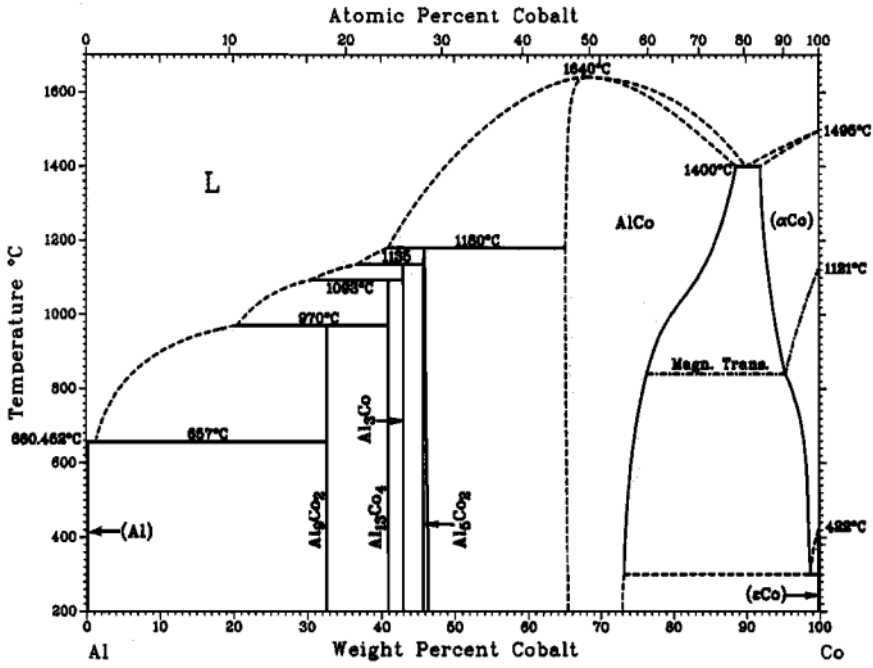

FIGURE 6.22

Equilibrium phase diagrams for Al-Co (*Source*: Reprinted from [242], courtesy of ASM).

researchers have attempted to avoid this problem by using a powder mixture of both pure Nb and Al powders with bulk composition in the range of 75% wt Al. Providing these powders mix and alloy to form a completely liquid melt pool, the melt pool temperature can be considerably lower (e.g., in the range of 1400 to 1600°C depending on the exact composition) even without dilution by the molten Al substrate surface. However, work by Almeida et al. [239] indicates that even under these circumstances complications arise.

Due to the high melting point of the Nb powder within the mixture, it is reasonable to assume that when these particles contact the melt pool surface they are still solid. Therefore, incorporation of these particles into the liquid state will require compositional dissolution of the Nb particles into the Al rich melt. Since there is essentially no solubility of Nb in liquid Al up to temperatures as high as 1400°C, this dissolution process is controlled by solid-state diffusion within the Nb rich particles. For example, when the Nb particle comes into contact with the melt pool, a diffusion couple develops between the two phases. Assuming that a pseudo-equilibrium develops, the intermetallic compounds depicted on the phase diagram can develop at the Nb/liquid interface. Thermodynamically, all of the phases can form between

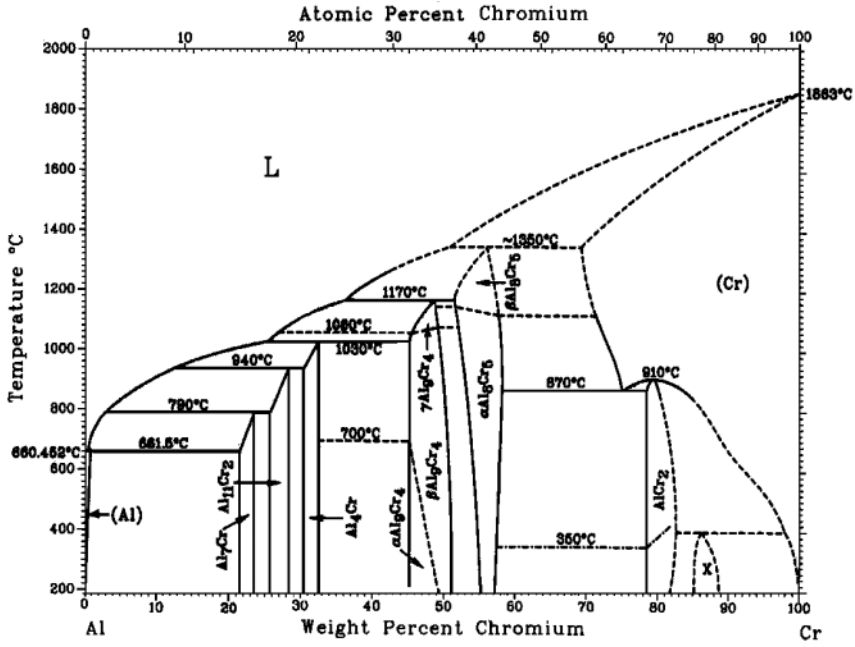

FIGURE 6.23

Equilibrium phase diagrams for Al-Cr binary alloys (*Source*: Reprinted from [242], courtesy of ASM).

the Nb particle and melt pool. However, the rate at which each layer grows will determine if the phase is detectable using characterization tools. The work of Almeida et al. indicates that in the Nb-Al system, Al_3Nb is the dominate intermetallic phase that forms under the laser cladding conditions they used. Dissolution of the Nb particle into the melt requires the migration of the solid/liquid boundary (as well as the other solid-state boundaries) toward the center of the particle. This, in turn, requires solid-state diffusion. This diffusion process is relatively slow compared to the liquid diffusion required to homogenize a full liquid melt pool. However the fine scale of the powders can minimize the time required for full dissolution. Calculations by Costa et al. [243] for the Nb-Al laser cladding conditions described above indicate that for 100 μm Nb particles, it would take 22 s for complete dissolution to occur. While this is a relatively short time frame for a solid-state process, it is much longer than the 0.24 s interaction time over which the melt pool is present at any position along the clad track [239]. In the case of Almedia et al.'s work, this results in a very nonhomogeneous clad microstructure with pores and undissolved Nb particles at the bottom of the clad zone suspended in a pure Al matrix (see Figure 6.25a) and a solidified structure at the top

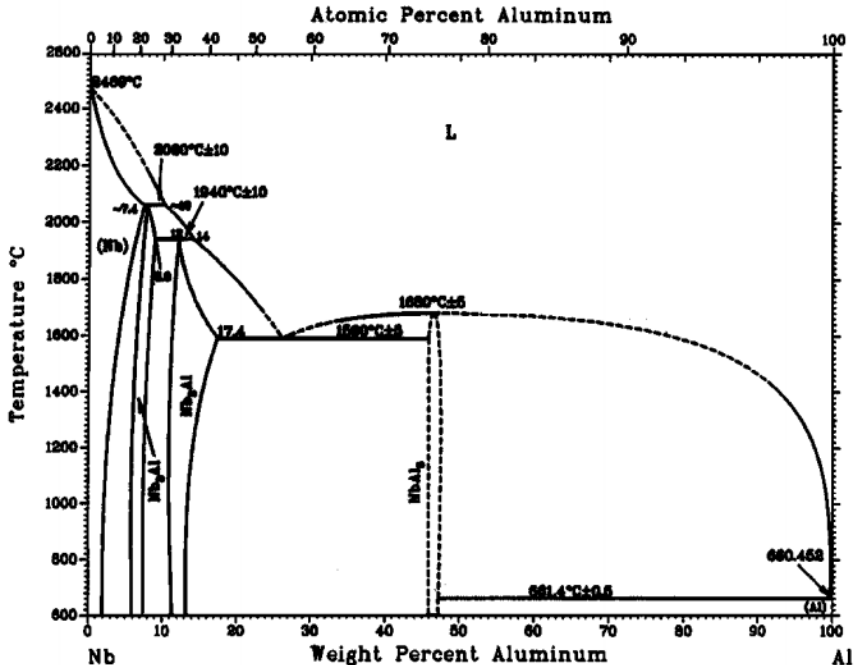

FIGURE 6.24

Equilibrium phase diagrams for Al-Nb binary alloys (*Source*: Reprinted from [242], courtesy of ASM).

of the clad consisting of Al_3Nb dendrites, also in pure Al matrix (see Figure 6.25b). The explanation offered for this is that undissolved Nb particles, with a higher density than liquid Al, sink to the bottom of the Al melt pool where very little or no convection forces are present (recall the calculation of Equation (6.1) in the previous section). The top layer of the clad obtains a liquid composition consisting of Nb and Al. Upon cooling, the top layer solidifies with the formation of primary Al_3Nb dendrites and a pure interdentric Al phase. This indicates that the composition of the melt pool was to the right of the Al_3Nb phase boundary in the phase diagram of Figure 6.24.

Because Al_3Nb is a brittle intermetallic compound [239], the bond strength of the Nb-Al clad system is not expected to be good. While bonding was not evaluated in detail, no cracking during processing or cooling was observed, and the intermetallic coating had an increased hardness compared to the Al substrate. The lack of cracking was attributed to the fine scale microstructure produced by the rapid solidification conditions of the laser cladding process.

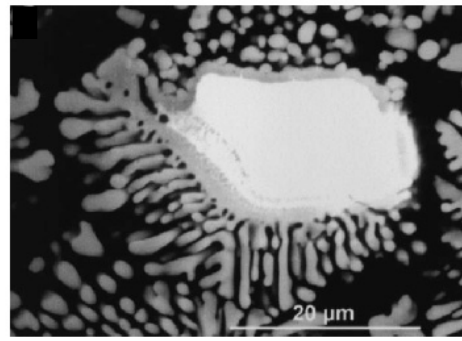

a)

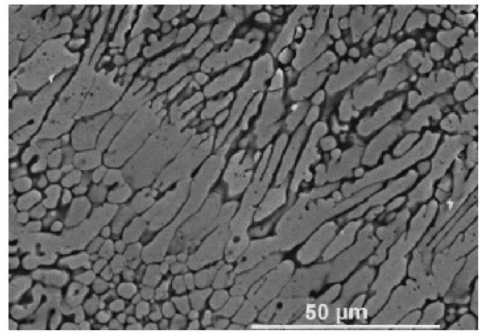

b)

FIGURE 6.25
Some Al-Nb clad microstructural features: a) an undissolved Nb (white) particle surrounded by Al_3Nb intermetallics phases (light grey) and suspended in a α-Al matrix (black), b) Al_3Nb dendrites (light grey) with interdendritic (black) α-Al (*Source*: Reprinted from [239], courtesy of Elsevier).

6.1.2.5 Case Study Cladding of Al on Mild Steel

In the above case, the general situation of a multi-component alloy system was considered, where the low melting point element was the substrate and the high melting point element (or a mixture made from it) was the powder. Another important general case to consider is the opposite situation (i.e., a high melting point substrate and low melting point powder). In this case, the initial requirement of low dilution is considered such that the bulk composition of the clad would be C_{o3} in Figure 6.21. Unlike the above case, melting of the powder should pose no problem due to its low melting point. However, the nature of alloying with the substrate during cladding can present problems which will be sensitive to the bulk composition of the formed clad. Some excellent examples of the problems that can occur [244] and some possible

solutions [245] are available for Al on mild steel. While mild steel does contain a small amount of C and Mn, over 98 wt% is Fe. Therefore, a qualitative understanding of the metallurgical interactions taking place can be achieved with the use of the Al-Fe binary phase diagram.

Inspection of the Fe-Al binary phase diagram of Figure 6.26 reveals that it is a complex, multi-component binary system with similar characteristics to the hypothetical phase diagram of Figure 6.21, and those of the other binary Al systems described above. As indicated by Figure 6.26, when Al alloys with the iron substrate, there is an increased melting (or liquidus) temperature compared to pure Al. In fact, the liquidus of the alloy sharply rises with a relatively small increase in Fe content. Therefore, maintaining a melt pool in this alloy will require laser energies that will be a function of the level of dilution by the substrate. On the other hand, melting of the substrate can be assisted by compositional dissolution by the Al-rich melt. This coupled with the lower melting point of Fe compared to Nb and higher solubility in liquid Al can result in the formation of a homogeneous and easily sustainable alloyed melt pool.

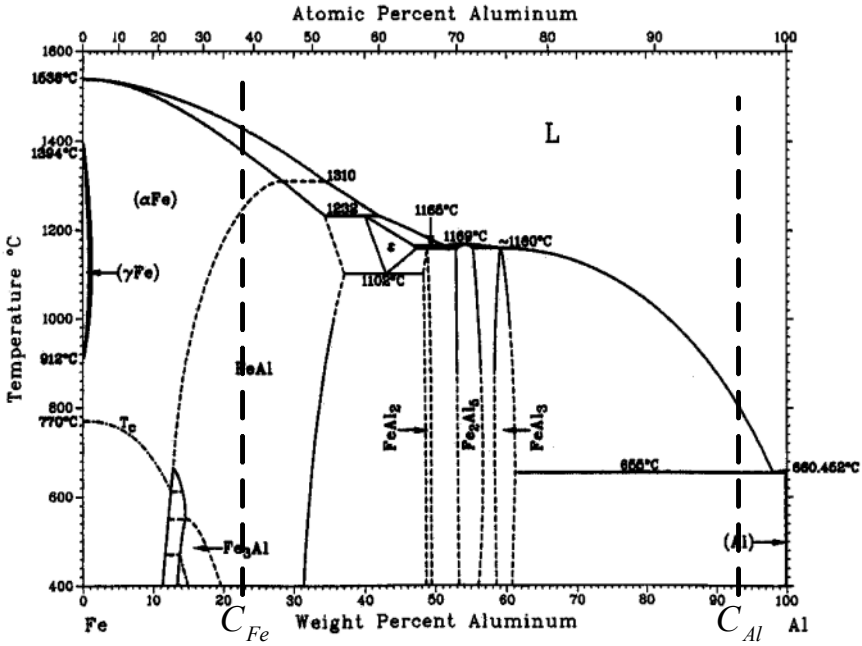

FIGURE 6.26

Equilibrium phase diagrams for an Al-Fe binary alloys (*Source*: Reprinted from [242], courtesy of ASM).

However, other problems are encountered in this clad couple as described by Ellis et al. [244]. With even a small amount of dilution of Al by the Fe from the mild steel substrate, the bulk composition of the melt pool will shift toward C_{Al} as indicated in the Figure 6.26. The solidification of Al-rich Fe melt pools under the rapid solidification conditions of laser processing has been studied in detail [204, 246]. While the phases that form during solidification depend on the melt pool temperature and composition as well as the solidification rate, primary dendrites of brittle Al_3Fe growing epitaxially from the substrate interface are difficult to avoid at Fe contents above 3 or 4wt%. This structure was observed by Ellis *et al* [244] and resulted in cracking of the substrate/clad bond during cooling and thus, poor cladability.

To attempt to overcome this problem, Ellis *et al* [244] placed several types of thin metallic coatings on the Fe substrate to prevent metallurgical interactions between Al and Fe. In the case of Cu coatings, the metallic layer completely alloyed with the melt pool leading to exposure of Al with the Fe below the coating. With the appropriate choice of laser processing conditions, a Ni coating remained in place while interacting with the melt pool. This effectively prevented interaction between Fe and Al. However, the metallurgical interactions that take place between Ni and Al, as the phase diagram of Figure 6.27 indicates, are similar to the Fe-Al system with the formation of an Al-rich Al-Ni melt pool. Ni_xAl_y intermetallic compounds grew from the substrate/melt pool interface during solidification. In the Ni-Al case, cracking did not occur during cooling. However, during bend tests, cracking and spallation of the clad coating from the substrate surface occurred. It was determined that this fracture process took place within the Ni-Al intermetallic layer. The final attempt by the researchers [245] was to coat the Fe substrate with an Al coating followed by laser cladding of Al powder. In this case, laser conditions were chosen where the Al coating was not completely melted. It was successful due to the elimination of the intermetallic phase formation on the clad/substrate interface.

Another possible solution to the cladding problem of Al on Fe is to alter the melt pool composition to avoid the formation of intermetallic compounds during solidification. This approach involves a powder mixture consisting of pre-blended pure Fe and pure Al powder, and a bulk composition of 18 wt% Al was clad onto a mild steel substrate. According to the Fe-Al phase diagram, the nominal melting temperature of this powder mixture is approximately 1450°C. Therefore, one of the advantages of this approach is that it brings the clad and substrate melting point temperature closer together, leading to better control over the laser cladding process particularly in the case of the level of dilution. Dilution levels near zero could be achieved with the appropriate laser processing conditions. The second advantage is that the diffusion couple setup between the steel substrate and melt pool produces no intermediate compounds and solidification of the melt pool takes place along the dashed line of Figure 6.26, labelled C_{Fe}. The solidification path does not lead to the growth of intermetallic compound but does result in

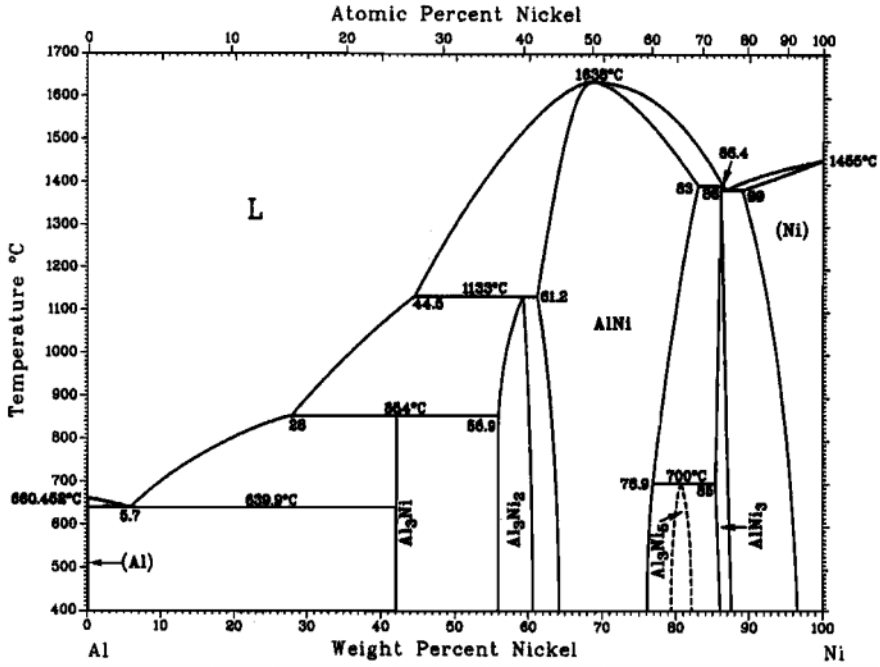

FIGURE 6.27

Equilibrium phase diagram of the Al-Ni binary alloy mixture (*Source*: Reprinted from [242], courtesy of ASM).

the solidification of α-Fe single-phase solid solution. Figure 6.28 illustrates a region of the solidified clad/substrate region. The clad microstructure consists of single phase columnar grains of FeAl solid solution. As discussed in section 6.1.1.1, this leads to a very strong bond between the clad and substrate.

6.2 Solidification Conditions Encounter in Laser Cladding

In Section 6.1, the metallurgical aspects of cladability were considered in detail. In particular, it was clearly demonstrated that alloying between the clad powder and substrate determines the melt pool composition. In addition, the phases that form during solidification, which are determined by substrate/clad alloying, play a major role in the development of the bond strength of the clad/substrate interface. In the Al binary alloy case studies discussed above, all three cases had an Al rich melt pool formed during cladding. Because the

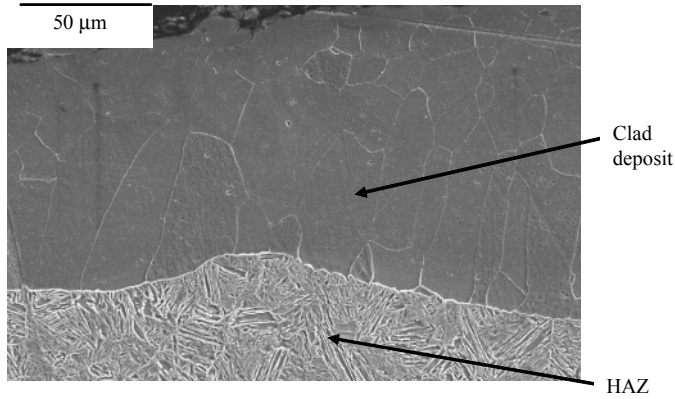

FIGURE 6.28

Microstructure of FeAl clad/substrate (steel) region for $\dot{m} = 2$ g/minute and $U = 2.0$ mm/s ($W = 10.5$ ms, $F = 30$ Hz, $r_l = 0.6$ mm, $P_l = 343$W).

nature of metallurgical interactions in the systems are similar, during solidification Al-Fe (or -Ni or -Nb) intermetallic compounds grow epitaxially from the substrate interface during solidification. However, despite these similarities, differences in the mechanical strength of the bonds formed do exist. For example, cracking during cooling was observed in the Al-Fe system, but not in the cases of Al-Ni or Al-Nb. Some of these differences are due to the different physical and mechanical properties of the intermetallics being formed (i.e., Al_3Fe, Al_3Ni or Al_3Nb) and the different thermal expansion mismatches that develop during cooling for the three clad/substrate couples. Another important influence is what types of microstructural features form during solidification. For example Ellis et al. [244] report that the Al_3Fe phase grows as a continuous layer at the clad substrate interface. This continuous brittle phase would be very susceptible to cracking during cooling. Work on the Al-Ni and Al-Nb couples indicate that the Al_3Ni or Al_3Nb grow as discrete primary dendrites perpendicular to the substrate interface. This type of structure would be less susceptible to cracking. In particular, Almeida et al. [239] attribute the lack of cracking in the Al_3Nb layer to be due to the formation of interdendritic $\alpha-$Al during solidification. This phase is soft and ductile and therefore contributes to an overall increase in the toughness of the Al_3Nb rich microstructure, making it much more resistant to crack propagation.

The above discussion points out that the nature of the microstructure that forms during solidification plays a very important role in determining the bond strength achievable during laser cladding. In addition, the microstructure that forms throughout the bulk of the clad deposition will also largely determine the physical and mechanical properties of the coating and therefore its suitability and performance in an application. For these reasons it

is extremely important to understand the conditions of solidification which can occur in laser cladding and the microstructures that result. This is the primary purpose of this section.

6.2.1 Process Conditions

Figure 6.29 illustrates a schematic of the process volume developed in laser cladding. Laser processing provides a localized heat source and a short interaction time (i.e., 0.5 s or less). This, coupled with the rapid heat removal by conduction into the substrate below the melt pool, leads to very rapid solidification rates (i.e., solid/liquid interface velocities as high as 1 to 2 m/s [247]). The heat removal is also very directional which sets up large positive temperature gradients (i.e., on the order of 10^6 K/m [247]) in the melt pool ahead of the solid/liquid interface.

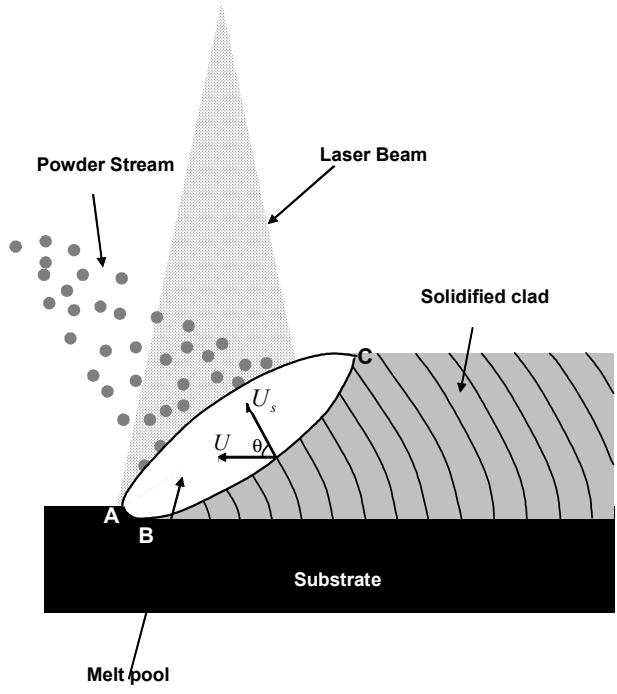

FIGURE 6.29
A schematic of the process zone during laser cladding. Melting takes place from A to B while solidification takes place from B to C. The lines within the solidified clad deposit indicate the direction of solidification.

The velocity of the solid/liquid interface U_s (i.e., rate of solidification) can be related to the scanning speed of the laser beam U (or in the case of a stationary beam, the velocity of the substrate), through the formula [247]

$$U_s = U \cos\theta \tag{6.2}$$

where θ is the angle between the vector representing the direction of the substrate motion and the vector normal to the solid/liquid surface at a particular point (i.e., the solidification rate).

Inspection of Figure 6.29 reveals that the solidification rate U_s varies throughout the process volume from zero at point B (where θ approaches 90°) to a maximum at the clad surface (where θ approaches 0°). Both the solidification rate and temperature gradient can be evaluated numerically, an example of which is given in Figure 6.30 for laser surface remelting [247]. The figure indicates the dependence of both solidification rate and temperature gradient G on the process speed. Also indicated is that the temperature gradient is highest at the bottom of the melt pool where U_s is zero and decreases toward the surface. This indicates that the solidification conditions vary throughout the melt pool. In order to understand how these processing conditions influence the microstructure that forms during solidification, the concept of constitutional supercooling must be described.

6.2.2 Constitutional Supercooling

Consider a simple eutectic alloy with a bulk composition of C_o and a binary phase diagram of Figure 6.31. Further, consider that solidification has achieved a steady state as described by Porter et al. [248], where the interface temperature has reached a constant temperature of T_1 (the solidus temperature for the bulk alloy), the solid/liquid interface is flat or planar and moving at a constant velocity U_s. In addition, it is assumed that solidification is proceeding at a fast enough rate that solid-state diffusion is negligible, and mixing in the liquid is limited to diffusional mass transport of solute in the liquid phase. Under these solidification conditions, the solute profile that develops across the solid/liquid interface is similar to that described in Figure 6.32a, where it is assumed that the interface compositions (and partition coefficient k_e) are determined by the equilibrium phase diagram. The width of the concentration profile in the liquid phase ahead of the solid/liquid interface has a characteristic width D/U_s which is dependent on the solidification rate and liquid phase diffusivity [248].

As the binary phase diagram indicates, the liquidus temperature is determined by the composition of the liquid. Since the solute composition changes near the solid/liquid interface so also does its liquidus temperature. The liquidus temperature as determined by the phase diagram for the liquid ahead of the solid/liquid interface is plotted in Figure 6.32b (i.e., curve marked T_L). Since the liquid composition varies from a maximum of C_o/k at the interface

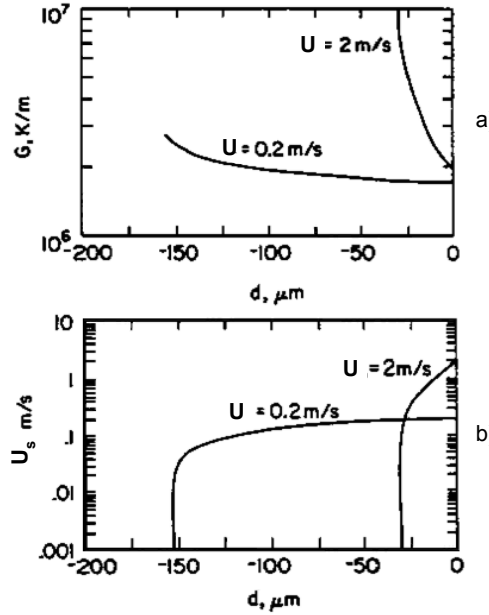

FIGURE 6.30

Calculated solidification conditions for laser surface remelting at two different process speeds: a) the temperature gradient, G_r, b) the solidification rate, U_s (d is the distance into the melted zone from the surface) (*Source*: Reprinted from [247], courtesy of ASME).

to C_o a short distance into the liquid, the liquidus temperature increases from T_1 at the interface to a constant value of T_2 a distance into the liquid [248].

In the case of laser cladding and many other solidification processes the "real" temperature gradient in the liquid ahead of the solid/liquid interface, G_r is positive as indicated in Figure 6.32b. The actual magnitude of G_r depends on the solidification conditions. If it is of the magnitude of that shown in Figure 6.32b, then a region of liquid ahead of the interface is known to be constitutionally supercooled. In other words, a certain portion of the liquid with elevated solute composition "experiences" a real temperature which is below its liquidus temperature determined by its composition. If a small protrusion develops at the interface its rate of growth will be larger than the bulk of the planar interface [248] in the constitutionally supercooled region. Therefore, its growth is promoted and the planar interface will become unstable. Depending on the degree of constitutional supercooling, the interface may develop a cellular structure or dendritic structure.

A critical temperature gradient G_c can be defined (see Figure 6.32b) above, which no supercooling occurs and the solidification front will remain planar.

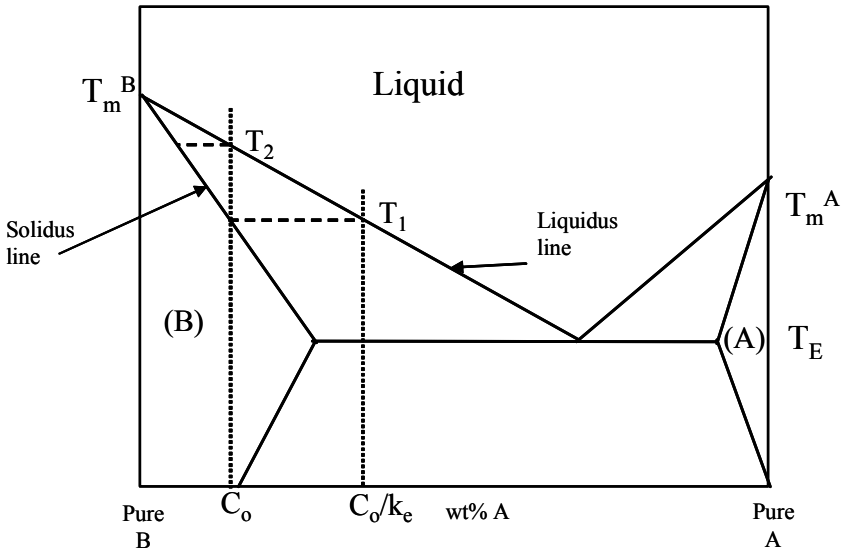

FIGURE 6.31

A schematic of a hypothetical phase diagram indicating steady-state solidification conditions.

Inspection of the figure reveals that the slope of this critical gradient can be defined as

$$G_c > \frac{T_2 - T_1}{D/U_s} \tag{6.3}$$

where $T_2 - T_1$ is known as the equilibrium freezing range for the alloy. Another form of Equation (6.3) is

$$(G_c/U_s) > \frac{T_2 - T_1}{D} \tag{6.4}$$

The left side of Equation (6.4) describes the important processing conditions present during solidification while the right side describes the material parameters of importance. It should be further noted that the magnitude of the equilibrium freezing range is determined by the equilibrium partition coefficient defined as

$$k_e = \frac{C_s}{C_l} \tag{6.5}$$

where C_s and C_l are the equilibrium solidus and liquidus compositions at T_1 (see Figure 6.31). When the value of k_e approaches unity this corresponds to solidus and liquidus lines that are close together, resulting in small freezing ranges.

From Equation (6.4), it can be stated that high temperature gradients and slow solidification rates will be more likely to avoid constitutional supercooling

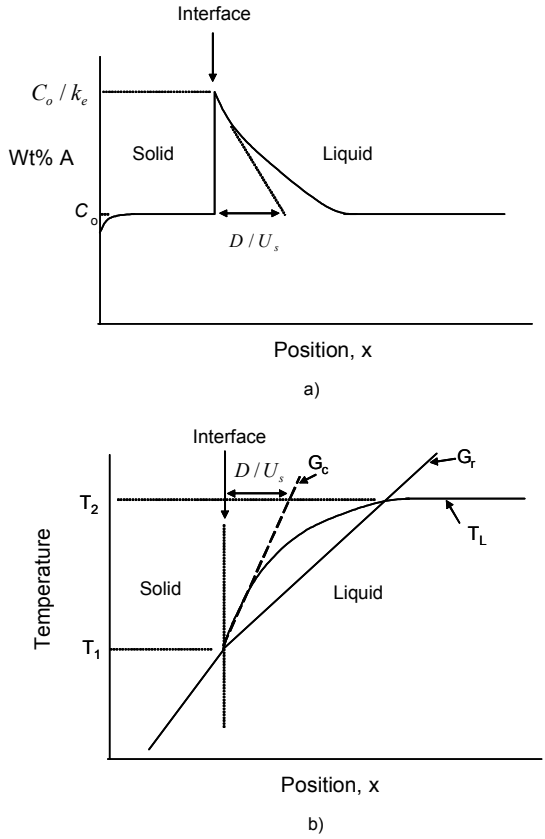

FIGURE 6.32

a) Compositional gradient, b) temperature gradient at the solid/liquid interface during steady-state solidification.

and favor a planar growth condition for a given alloy system. Alternatively, alloys with small freezing ranges will be more likely to solidify with a planar front under moderate values of G_r and U_s.

Applying these concepts to laser cladding, it can be stated by inspection of Figures 6.29 and 6.30 that at the base of the clad layer, region B, (G_r/U_s) is at a maximum and therefore solidification by a planar front would be favored in this location. On the other hand, (G_r/U_s) are at their lowest at the surface, region C. Therefore, a transition from planar solidification to dendritic growth from the clad deposit near the substrate interface to the clad surface would be expected. Figure 6.30 also illustrates that the change in the ratio of (G_r/U_s) per unit length of the melt pool depth is more significant at higher laser processing speeds.

An excellent example of how these changing (G_r/U_s) values alter the microstructure in a clad deposit is given by Vilar [249] for a Stellite 6 clad deposit. At the base of the clad near the substrate surface, a microstructurally featureless zone indicates a region of plane front solidification. This type of zone has been observed by many researchers [247]. The microstructure then transforms to a cellular structure and then finally a fully developed dendritic structure with secondary dendrite arms.

6.2.3 Rapid Solidification

Many complex engineering alloys have a significant equilibrium freezing range and therefore dendritic growth is often the dominant solidification process and therefore most common microstructural feature observed in the clad deposit. This is due to the difficulty in meeting the criterion of Equation (6.4) for a planar form when $[T_2 - T_1]$ is relatively large. However, with increasing solidification rates the compositions in the solid and liquid at the tip of the dendrites no longer follow their equilibrium values. This is because the atoms do not have the time to diffuse and maintain local equilibrium at the solid/liquid interface. One primary way in which to describe this effect is through the use of the solidification rate dependent partition coefficient k_v [250]

$$k_v = [k_e + a_o U_s/D]/[1 + a_o U_s/D] \tag{6.6}$$

where a_o is a characteristic value of the thickness of the interface and the other parameters are as defined above. As the solidification rate U_s increases, k_v approaches unity. Kurz et al. [247] have applied non-equilibrium solidification modelling to an Al-4%Cu alloy to determine the concentrations in the solid and liquid (i.e., C_S^* and C_L^* , respectively) at the dendrite tip as a function of temperature for high solidification rates. Figure 6.33 plots these results. Also included are the equilibrium solidus and liquidus lines. The fine dashed line shows the values of C_S^* and C_L^* as a function of temperature. At low undercoolings (and therefore low solidification rates), the non-equilibrium values follow closely the equilibrium lines. However, with increasing undercoolings, they deviate significantly. Also plotted in the figure are the effective solidus and liquidus lines at a solidification rate of V_a, which Kurz and Trivadi [247] define as the absolute stability point. Clearly, the value of k_v is significantly closer to unity than the equilibrium partition coefficient and therefore the effective freezing range of the alloy is considerably reduced. According to the criterion of Equation (6.4), this could lead to the re-establishment of a stable, planar interface at high solidification rates.

This phenomenon has been modelled by Kurz and Trivadi [247], the results of which, for Al-4%Cu, are presented in Figure 6.34. Clearly the type of microstructure that develops depends on both the solidification rate and temperature gradient. A region of planar growth (P) exists at both low and high growth rates but does depend on the temperature gradient at low values

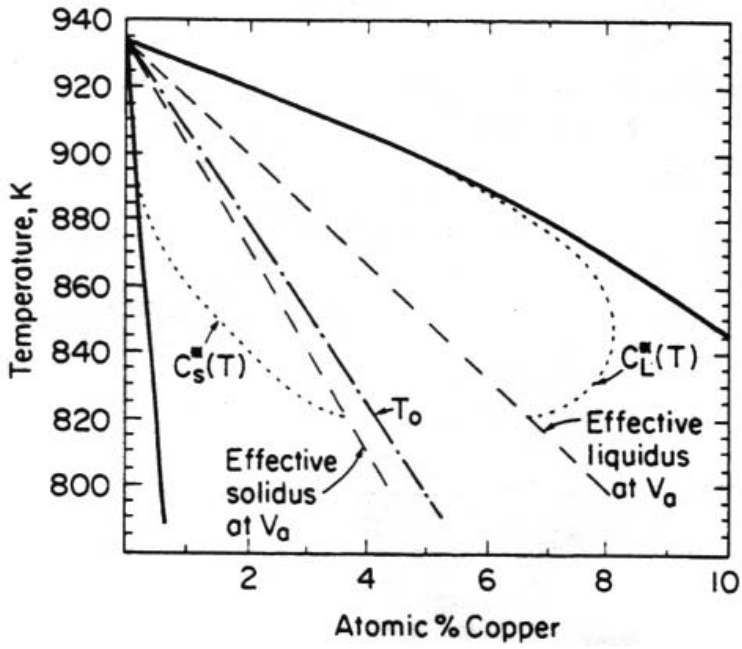

FIGURE 6.33
Calculated compositions in the solid and liquid (C_S^* and C_L^*, respectively) and effective solidus and liquidus lines for an Al-Cu alloy as a result of rapid solidification. V_a is the solidification rate corresponding to the absolute stability point. Solid lines indicate the equilibrium solidus and liquidus lines (*Source*: Reprinted from [247], courtesy of ASME).

of U_s. At intermediate growth rates, non-planar growth, in the form of cells or dendrites, exists (see Figure 6.34b). Included in Figure 6.34a are the laser surface remelting traces of Figure 6.30. Based on these traces, one would predict a planar structure near the substrate interface followed by a cellular region and then dendritic structure. At very high rates the planar solidification front can also be replaced by a banded structure. This type of transition has been observed in Al-Cu [251] and Al-Fe [246] binary systems.

6.2.4 Microstructure Maps

From the above discussion, it is clear that both the laser cladding processing conditions, which determine the values of G_r and U_s with the melt pool, and the alloy composition, which determines the magnitude of the freezing range (or the values of k_e and/or k_v), will determine the type of microstructure formed in the clad layer during solidification. The case studies of Al-Nb,

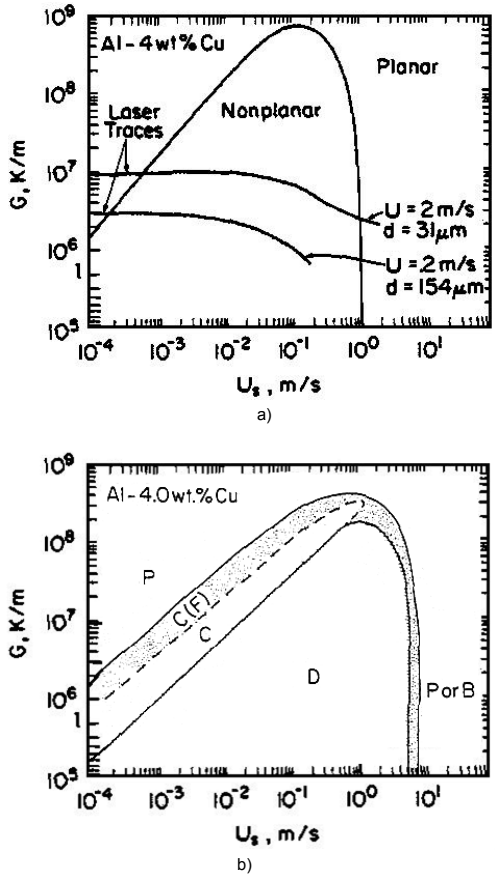

FIGURE 6.34

Mode of solidification and the resultant microstructure as a function of the temperature gradient G_r and solidification rate U_s, a) including laser conditions, b) including type of non-planar growth. P-planar, C(F) and C-cellular, D-dendrites and B-banding (*Source*: Reprinted from [247], courtesy of ASME).

Al-Ni and Al-Fe given in Sections 6.2.2.1 and 6.2.2.2 illustrate that this microstructure can have a large impact on the substrate/clad bond strength, and thus the success of the cladding process. It would, therefore, be extremely useful to be able to predict what microstructures would develop under certain processing conditions so that the optimum microstructure could be selected by the appropriate choice of laser processing parameters. Several researchers [204, 246, 251, 252] have developed microstructural maps with the aim of providing this type of information. An example of such a map is given in Figure 6.35 for an Al rich binary Al-Fe alloy. Similar maps have also been developed for Al-Cu alloys [251] and Ag-Cu [252]. The solid lines in the figure indicate results of experimental observations, whereas the dashed lines indicate calculated values from solidification models.

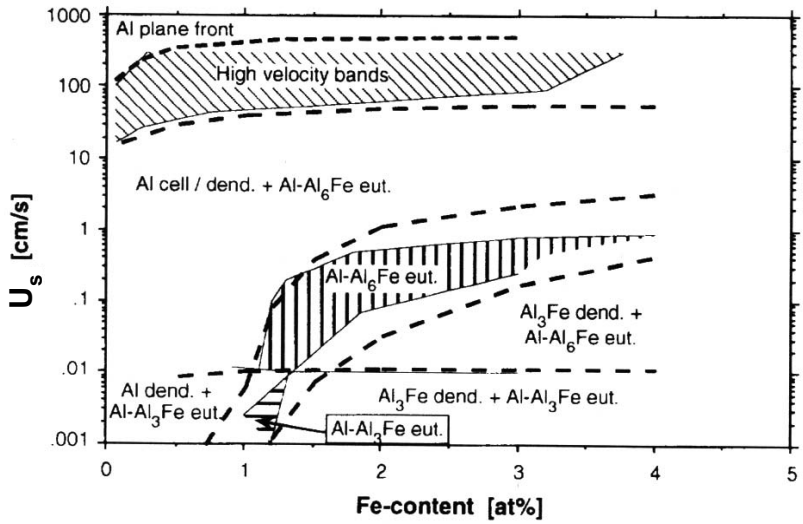

FIGURE 6.35
The type of microstructure observed (solid lines) and predicted (dashed lines) in an Al-Fe binary alloy as a function of solidification rate and Fe content (*Source*: Reprinted from [246], courtesy of Elsevier).

At low Fe contents and slow solidification rates, primary dendrites of $\alpha-$Al with interdendritic regions of equilibrium eutectic (Al-Al_3Fe) are the preferred microstructure. As the solidification rate increases, a similar microstructure develops except that the equilibrium (or stable) eutectic is replaced by a metastable Al-Al_6Fe eutectic. The formation of metastable phases during rapid solidification has been observed in other alloy systems [240, 253, 254,

255]. With a further increase in the solidification rate, the condition for absolute stability of the solid/liquid interface is approached with the formation of a banded and then plane front structure.

With an increase in the Fe content, the sequence of microstructural development as a function of solidification rate changes. In the slow to moderate range, the preferred microstructure changes from primary dendrites of $\alpha-$Al with interdendritic Al-Al_3Fe (or Al-Al_6Fe), to an all eutectic Al-Al_3Fe (or Al-Al_6Fe) structure and then finally to primary dendrites of Al_3Fe with interdendritic Al-Al_3Fe (or Al-Al_6Fe). At very high solidification rates, the microstructure that forms becomes insensitive to the Fe content where banding or a plane front becomes the preferred structure. What this diagram points out is that with a careful control over the process parameters, including dilution by the substrate (or clad composition), a range of microstructures for the clad can be selected. In the particular case of the problems encountered by Ellis et al. [244] for an Al cladding on Fe, the problems encountered with the formation of brittle Al_3Fe dendrites at the surface may be avoidable if the level of Fe in the cladding (and thus dilution) could be kept to a minimum.

Microstructure maps similar to Figure 6.35 are not yet available for more complex ternary and higher order alloy systems. However, the work of Kurz and others points out the tremendous value of these maps and the importance of developing them for other systems.

6.2.5 Microstructural Scale

Another consequence of rapid solidification is that it causes a refinement in the microstructure of the as-cast material. In the case of cellular or dendritic growth, this can be understood by referring to Figure 6.32. As the solid grows it must reject solute into the liquid ahead of the solid/liquid interface. With the formation of a cellular or dendritic structure, solute can be more efficiently rejected in lateral directions as well as in front of the tip. As the solidification rate increases, the need to reject this solute more effectively increases and the dendrite tip radius becomes smaller. This results in a refinement in the dendrite spacing and overall microstructure. An example of how the laser processing speed can be used to refine the clad microstructure (through an increase in solidification rate) is given in Figure 6.36 for the cobalt-based Stellite 6 alloy [80]. At a slow scanning speed of 1.67 mm/s, the secondary dendrite arm spacing λ_s is in the range of 2.5 to 6 μm, whereas at a scanning speed of 167 mm/s, λ_s is reduced to 0.5 to 0.8 μm.

Because the solidification rate varies from near zero to a maximum at the clad surface, it is expected that the microstructure of the clad should also be refined across its height. An example of this refinement is given in Figure 6.37 for an Al-Si-Ni clad material placed onto an Al-Si substrate [256]. In this case, solidification of primary dendrites of Al_3Ni_2 and/or Al_3Ni (the white phase in the figure) with interdendritic Al-Al_3Ni are the dominant microstructural features. A clear refinement in the scale of the dendrites is visible in going

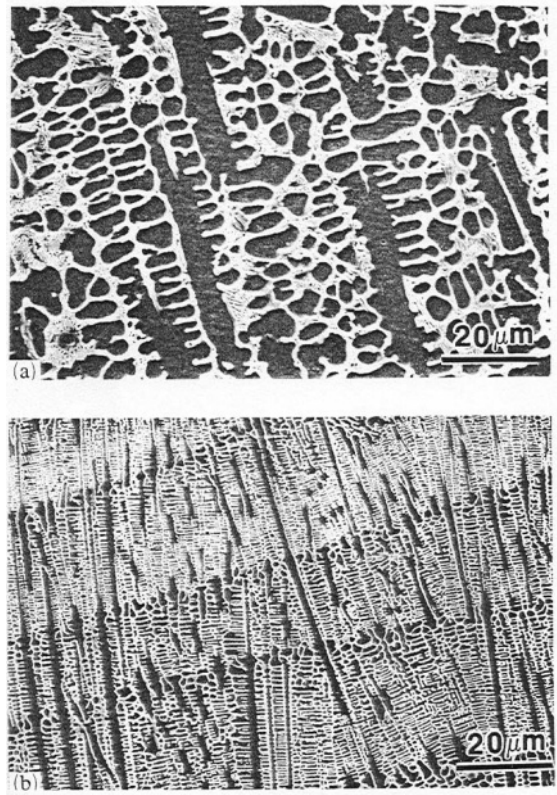

FIGURE 6.36
Microstructure of a Co-based Stellite 6 clad deposit at a) a laser scanning speed of 1.67 mm/s, b) a laser scanning speed of 167 mm/s (*Source*: Reprinted from [80], courtesy of Elsevier).

from the bottom to the top of the clad.

Gilgien et al. [246] have constructed a microstructure map for Al-Fe which includes the dendrite tip radius (or in the regions where eutectic forms, the interphase spacing). A clear correlation exists between solidification rate and microstructural scale (see Figure 6.38). This diagram also illustrates the great potential that laser cladding has in producing nanoscaled microstructures. These ultra-fine microstructures, the finest of which will be located at the clad surface, are in large part the reasons for the high hardness values or increased wear resistance so often reported in laser cladding research [35, 239, 247, 249, 253, 254, 256, 257].

An additional consequence of rapid solidification is the development of extended solid solubility. This can be understood with reference to Figure 6.33.

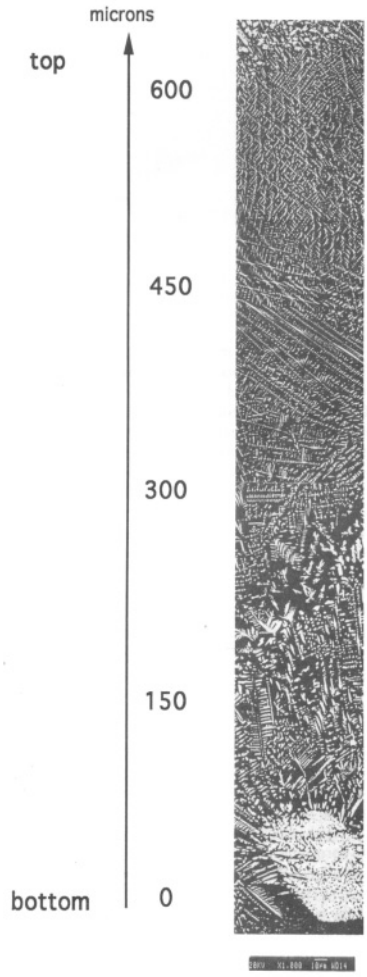

FIGURE 6.37
Microstructure of an Al-Si-Ni clad on an Al-Si substrate showing the scale of the primary Ni aluminide dendrites (white phase) as a function of the clad depth (*Source*: Reprinted from [256], courtesy of Elsevier).

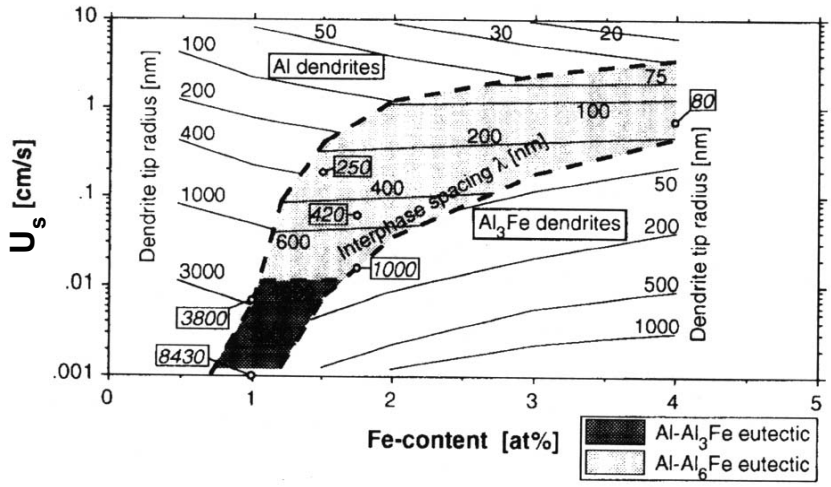

FIGURE 6.38
Scale of the solidified microstructure of laser remelted Al-Fe as a function of solidification rate and Fe content (*Source*: Reprinted from [246], courtesy of Elsevier).

As the solidus line shifts to the right of the equilibrium case, more solute remains in solid solution within the primary phase. This phenomenon has been investigated by a number of researchers in systems including Ag-Cu [252], Nb-Al [241], and Ni-based alloys [51, 49, 160]. Solubility increases can be as high as several percent. This increased solubility will lead to higher levels of solid solution strengthening and contributed to increase hardness and strength in the clad material.

Accompanying the non-equilibrium solute content is the formation of metastable phases such as the Al_6Fe based eutectic illustrated in Figure 6.35. The formation of metastable phases have been observed in Ni-based, Co-based, and Fe-based alloys mostly in the form of metal carbides and/or borides [253, 254, 255]. Again, these metastable phases will have an impact of the mechanical properties of the clad deposit.

6.3 Material Systems Used in Laser Cladding

There has been a rapid increase in research activities related to laser cladding, growing from a handful of published journal papers in the 1980's to over 60 in the year 2003. A wide range of materials have been studied, and it

can be safely said that the feasibility of laser cladding using every major class of metallic alloy as well as ceramics, glasses and intermetallics has been investigated. Alloy systems that have been laser clad include Ni, Co, Nb, Ti, Al, and Cu-based alloys as well a full range of steels including tool and stainless steels. However, over the past several years, two general material systems have enjoyed particular attention and will be the focus of this section.

By its nature, the major objective of laser cladding is to create a high performance surface with enhanced properties including wear resistance, corrosion resistance, and/or oxidation resistance. Traditionally, materials with these high performance attributes are high temperature materials, which are expensive and difficult to process in bulk form. Therefore, creating a coating of these materials on less expensive, easily processed base materials is where laser cladding offers the best advantages.

6.3.1 High Temperature Alloys

Over the span of the last 20 years there has been a major emphasis on the laser cladding of high temperature Ni, Co and/or Fe-based alloys. These alloys are generally expensive and difficult to process by conventional means but offer superior properties. In the majority of cases, these alloys are clad onto relatively less expensive low carbon or low alloy steels [75, 112, 77, 81, 253, 254, 255, 109, 112, 79]. The main alloying elements in most of the clad alloys include Ni, Co, Cr and Fe with smaller amounts of W and Mo as well as C, which forms metal carbides with the alloy ingredient. Generally, these alloys exhibit good cladability with low carbon steel substrates. This can be qualitatively understood in light of the discussion of Section 6.2.2 by realizing that Fe is very soluble in Ni, Co, and Cr in the solid-state near the melt pool temperatures with no intermetallic phases forming between the constituents during solidification. However, this general statement can be complicated by complex alloy compositions and with the presence of C, B and W. Metal carbides can form during solidification and brittle, intermetallic compounds can precipitate in the solid-state during cooling. Therefore, hot and cold cracking can take place in the deposit/substrate during laser cladding [258]. Often pre- and/or post-heat treatments are required to avoid these problems. However, a detailed discussion of these problems is beyond the scope of this text.

Another common application of laser processing using high temperature alloys is the cladding of Ni-based substrates with Ni-based cladding containing rare earth elements such as Hf [77, 259, 260, 261]. In these cases the high temperature oxidation resistance of Ni-based superalloys can be improved by the rare earth additions. In these cases, since the clad composition is only slightly different than the substrate, cladability is generally very good.

6.3.2 Composites

Since a primary application of laser cladding is to create a hard wear-resistant surface, it is not surprising that a significant research effort is being made to laser clad metal/ceramic composite coatings onto metal substrates [262, 263, 264, 265, 266, 267, 268, 269, 270]. Metal/ceramic composite (MCC) materials are relatively difficult to process by conventional means such as powder metallurgy or ingot metallurgy, particularly when high ceramic volume fractions are required [271]. These composites also tend to have low ductility and fracture toughness, making them unsuitable in bulk form for many applications [272]. However, by virtue of their ceramic content they exhibit high hardness and excellent wear resistance. Therefore, their use in laser cladding is an ideal application [262, 263, 264, 265, 266, 267, 268, 269, 270].

Generally, there have been two approaches to the cladding of MCCs. In the first, ceramic particles, (sometime with metallic binders) are mixed with metal particles and added to the melt pool either by pre-placement on the substrate or by powder injection [262, 263, 264]. In these investigations, the goal is to limit the reaction between the ceramic particles and the metallic melt pool. WC particles are the ceramic particles of choice in this approach because they seem to be resistant to dissolution into the melt pool. The problems encountered during this process are similar to those encountered in more conventional ingot metallurgy techniques for producing MCCs [272, 273]. The ceramic particles must wet the liquid metal in order to be incorporated into the melt pool. However, there must not be an extensive deleterious reaction taking place between the particle and alloying elements with the metallic liquid. In addition, during solidification particle pushing can lead to inhomogeneous distributions of the ceramic particles within the metal matrix. These problems are only just beginning to be evaluated in laser cladding [263]. In cases where TiC and SiC are used as the ceramic particle, reaction does take place with the metal powder [71, 265, 266]. For example, when SiC and Ni are combined, nickel-silicide compounds form [265] and for TiC and Al, titanium-aluminide compounds form [71].

The reactions that take place between the ceramic particles and melt pool are not necessarily negative for either cladability or wear resistance. In fact, in a second approach, ceramic reinforcement is developed by in-situ reactions between the powder ingredients within the molten zone. [265, 266, 267, 268, 269, 270]. In some cases, ceramic particles are added to the clad deposit and undergo partial or complete dissolution into the melt pool and re-precipitate during solidification [265, 274]. In other cases elemental powders are added to the melt pool and then react to form the reinforcing phase. Examples of this include the addition of Mo, Si and C powders which form $MoSi_2$ and SiC particles [267], the addition of Ni-based alloy and Zr powder to form ZrC particles [269], and Ni-based alloy, graphite and Ti powder to form TiC particles [270]. The advantages of this approach include the formation of fine ceramic particles that are well bonded to the matrix. As Figure 6.39 indicates,

a large increase in hardness can result from the in-situ formation of the laser clad MCCs. This fairly new approach to laser cladding shows great potential for the creation of novel materials with unique properties.

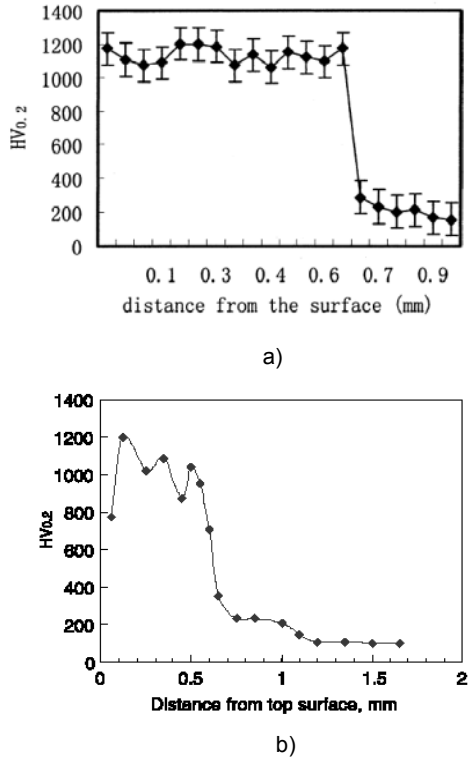

FIGURE 6.39

Vickers microhardness readings across clad/substrate couples: a)in-situ formation of ZrC MCC clad on a mild steel substrate, b) in-situ formation of $MoSi_2$ and SiC MCC clad on a commercially pure Al substrate (*Source*: preprinted from [269] and [267], respectively, courtesy of Elsevier).